



Studying the effect of sea spray using large eddy simulations coupled with air–sea bulk flux models under strong wind conditions

Panagiotis Portalakis¹ · Maria Tombrou¹ · John Kalogiros² · Georgia Sotiropoulou¹ · Julien Savre³ · Annica M. L. Ekman⁴

Received: 21 June 2023 / Accepted: 17 August 2024

© The Author(s), under exclusive licence to Springer-Verlag GmbH Austria, part of Springer Nature 2024

Abstract

Three high resolution large eddy simulations (LES) with two bulk air–sea flux algorithms, including the effects of water phase transition, are performed in order to study the influence of sea spray on the marine atmospheric boundary layer (MABL) structure and cloud properties. Because sea spray has a notable impact under severe wind conditions, the CBLAST-Hurricane experiment supplies the initial realistic conditions as well as turbulence measurements for their assessment. However a hurricane boundary layer (HBL) simulation is not in the scope of this study. Although the simulations in the final state depart from the initial conditions, all three momentum flux distributions are found at the low end of the observed range. The spray-mediated sensible heat flux is opposite to the interfacial flux and reaches up to 60% of its magnitude. When the spray-mediated contribution is taken into consideration, the simulated moisture flux increases by up to 45% and gets closer to the observations. Small scale stream-wise velocity streaks are arranged, probably due to spray effects, into large scale structures where the scalars' variations tend to concentrate. However, the vertical velocity structure below mid-MABL is not greatly affected as the buoyancy forces locally within these structures are negligible. Spray effects greatly enhance the magnitude of the quadrant components of the scalar fluxes, but the net effect is less pronounced. Spray-mediated contribution results in more extended cloud decks in the form of marine stratocumulus with increased liquid water content. The visually thicker clouds reduce the total surface radiation by up to 30 Wm^{-2} .

1 Introduction

Large eddy simulations (LES) are considered a critical tool for atmospheric scientists in order to understand the atmospheric boundary layer (ABL) dynamics. This high accuracy approach has undergone multiple enhancements since it

was initially implemented by Deardorff (1970). It explicitly resolves the turbulent structures carrying most of the kinetic energy, whilst smaller filtered structures are modeled. These smaller structures (subgrid scales) typically carry only a relatively small portion of the kinetic energy and mainly dissipate energy transferred from the larger scales.

Energy exchange at the marine atmospheric boundary layer (MABL) air–sea interface is one of the most important

Responsible Editor: Clemens Simmer, Ph.D.

✉ Panagiotis Portalakis
pportal@phys.uoa.gr

Maria Tombrou
mtombrou@phys.uoa.gr

John Kalogiros
jkalog@noa.gr

Georgia Sotiropoulou
georgiasot@phys.uoa.gr; georgia.sotiropoulou@epfl.ch

Julien Savre
julien.savre@lmu.de; Julien.Savre@physik.uni-muenchen.de

Annica M. L. Ekman
annica@misu.su.se

¹ Department of Environmental Physics and Meteorology, Faculty of Physics, National and Kapodistrian University of Athens, Athens, Greece

² Institute of Environmental Research and Sustainable Development, National Observatory of Athens, Athens, Greece

³ Meteorological Institute, Faculty of Physics, Ludwig-Maximilians-University Munich, Munich, Germany

⁴ Department of Meteorology, Bolin Centre for Climate Research, Stockholm University, Stockholm, Sweden

physical components of Earth's climate and its variability. Enormous amounts of heat, moisture and momentum are transported across this interface mostly by turbulence. This energy exchange affects from the maintenance of stratocumuli (Bretherton and Wyant 1997) to how hurricanes intensify (Andreas and Emanuel 2001; Black et al. 2007; Emanuel 1991; Wang et al. 2001).

On average, low-level clouds, particularly stratocumuli cover 23% of the ocean surface each year (Wood 2012). Thus, they constitute an important climatological component as the cloud cover can modify the solar radiation which reaches the Earth's surface. Turbulent fluxes affect the structure and evolution of the cloud-topped MABL. Furthermore, radiative cooling, evaporative cooling, and entrainment rates are all strongly connected processes which produce and are driven by turbulence and, thus, they influence the development and evolution of cloud layers as a whole (Mellado 2017; Rauterkus and Anson 2020). For instance, radiative cooling promotes convective instability, which is a primary mechanism of turbulence generation that enhances the entrainment of dry air from aloft. This dry air mixing in the MABL can change the near-surface moisture and, hence, the latent heat flux (Zheng et al. 2018). Therefore, when simulating the MABL with LES the impact of cloud microphysics and radiation processes must be considered, as these processes closely interact with one another and turbulence.

The interest in wind-wave interaction first emerged in the latter half of the twentieth century (Large and Pond 1981; Wu 1982; Yelland and Taylor 1996). The main goal of their research was to determine the surface total wind stress (or drag coefficient) using in-situ observations in most cases up to moderate wind conditions and parameterize it using the neutral wind speed at 10 m, U_{10m} , above the mean sea level (amsl). This simplification, however, implicitly includes the effects of various parameters of sea state and other processes, including wave breaking, the subsequent airflow separation, and formation of sea spray by bubble bursting or direct surface detachment at high winds conditions. Thus, the individual contribution of each process to the wind stress or heat fluxes could not be quantified.

The dependence of stress (momentum flux) on wind velocity was usually extrapolated to high wind conditions, yielding a parameterization of drag coefficient that grows linearly with wind speed. Recent research has challenged this approach, confirming that in hurricane-force winds the surface drag coefficient saturates or even decreases (Bell et al. 2012; Donelan 2004; Powell et al. 2003). The theoretical explanation for drag leveling-off includes the "sheltering effect" and the air-flow separation between consecutive wave crests, which results in the air-flow not feeling the actual sea roughness (Kudryavtsev and Makin 2007; Kukulka and Hara 2008; Kukulka et al. 2007; Mueller and Veron 2009). In addition, the surface drag can be affected by the

development of a foamy layer smoother than the actual surface (Donelan 2004; Holthuijsen et al. 2012; Powell et al. 2003), and by changes in the near-surface wind speed due to redistribution of horizontal momentum by the falling sea-spray droplets (Kudryavtsev 2006; Makin 2005; Richter and Sullivan 2013).

Sea spray droplets lofted into the air increase the effective contact area between the ocean and the atmosphere, offering an additional mechanism in strong wind conditions for the exchange of heat fluxes, i.e. sensible and latent heat. Veron (2015) and Sroka and Emanuel (2021) present a thorough analysis of this topic while addressing the advancement of spray heat transfer modeling over the last few decades as a result of theoretical, observational, and numerical modeling approaches. Sea spray modeling employs bulk algorithms, Eulerian and/or Lagrangian approaches (Andreas et al. 2015; Bao et al. 2011; Kepert et al. 1999; Mueller and Veron 2014a, b; Peng and Richter 2017, 2019; Richter and Wainwright 2023; Shpund et al. 2012, 2014).

Two approaches are commonly used for the surface boundary conditions when simulating the MABL using LES. The first considers the air-sea interface to be a solid rough surface, with the waves being characterized as roughness elements. The Monin-Obukhov Similarity theory (MOST) framework is used and the surface shear stress is parameterized with a bulk aerodynamic method based on wind speed (Andreas et al. 2012; Foreman and Emeis 2010) or on information about the wave field. These wave data are either provided in the form of bulk variables like wave-age and wave-steepness (Drennan 2003; Edson et al. 2013; Taylor and Yelland 2001), or obtained from wave spectra (Hara and Belcher 2004; Janssen 1989; Makin and Kudryavtsev 1999; Moon 2004). The second approach couples the turbulent boundary-layer flow to the sea surface via a time-varying waving boundary condition (Hao and Shen 2019; Hara and Sullivan 2015; Sullivan and McWilliams 2010; Sullivan et al. 2000, 2008, 2014, 2018; Yang et al. 2013). This solid boundary is either moving in a prescribed fashion or in response to the airflow. However, these wave-resolving LES are highly computationally demanding, with requirements which exceed today's typical high-performance computing resources, especially when microphysics and radiation are considered (Hao and Shen 2019).

Our main goal is to improve MABL representation by incorporating the air-sea interaction mechanism into an LES code which already includes the effects of water phase transition, cloud microphysics, and radiation processes. The MISU MIT Cloud and Aerosol (MIMICA) LES model for cloudy ABL (Savre et al. 2014) is employed, which is extended to include two bulk air-sea flux algorithms, namely COARE 3.5 (Edson et al. 2013; Fairall et al. 2003) and Andreas' latest version 4.0 (Andreas et al. 2015). Realistic data from the CBLAST-Hurricane experiment (Black et al. 2007) during

hurricane Isabel on 12 September 2003 are used to initialize the model and validate our results, as it is one of the few datasets which include strong winds and turbulence measurements. We do not attempt to actually simulate a HBL, therefore the large-scale pressure gradient and meso-scale tendencies like advection and centrifugal force are not taken into consideration (Bryan et al. 2017; Worsnop et al. 2017). We analyze the impact of sea spray on the surface fluxes and, thus, on MABL structure and cloud macro-physical properties under severe wind conditions.

2 Methodology

Over the ocean, there is additional stress induced by the wave form in addition to the stress caused by viscous boundary effects and turbulence (Belcher and Hunt 1993; Edson and Fairall 1998; Hare et al. 1997; Janssen 1989; Makin et al. 1995). The form stress is caused by the interaction between air-flow and waves and can be further divided into non-breaking (regular waves) and breaking waves (inducing air-flow separation) (Kudryavtsev and Makin 2001). Various studies have also examined the potential impact of sea spray on stress (Andreas 2004; Kudryavtsev and Makin 2011; Makin 2005). These stress components vary with height with the total stress τ considered constant in the surface layer. The bulk aerodynamic method is used for the parameterization of total stress, τ , and reads:

$$\tau = \rho C_{dz} U_z^2 \tag{1}$$

where ρ is the air density and U_z is the wind velocity at height z ; C_{dz} , is a non-dimensional drag coefficient which is related to the momentum roughness length, z_o , through the logarithmic profile (Stull 1988). For non-neutral atmospheric stability conditions, the drag coefficient at $z = 10$ m is given by:

$$\sqrt{C_{d10}} = \frac{u_*}{U_{10}} = \frac{\kappa}{\ln(10/z_o) - \psi_m(10/L)} \tag{2}$$

where $u_* = \sqrt{\tau/\rho}$ is the friction velocity, κ is the von Karman constant, ψ_m is a dimensionless function which accounts for the effects of atmospheric stratification and L is the Monin–Obukhov length. Following Smith (1988), the momentum roughness length is expressed as:

$$z_o = z_o^{smooth} + z_o^{rough} \tag{3}$$

where z_o^{smooth} accounts for an aerodynamically smooth flow (for $U_{10} < 2 \text{ ms}^{-1}$) where viscous stress dominates, while z_o^{rough} accounts for the rough flow (for $U_{10} > 8 \text{ ms}^{-1}$) where the momentum transferred by turbulent eddies interacting with the waves dominates. The term, $z_o^{rough} = \alpha u_*^2/g$ was introduced by Charnock (1955) where g is the gravitational

acceleration and α is the Charnock coefficient, which is usually expressed as a function of sea state in terms of wind speed, wave age or wave steepness or other wave-related parameters.

Similarly to momentum, the scalar transfer coefficients for sensible heat, C_{t10} , and latent heat, C_{q10} , are related to the scalar roughness length z_{ox} (x stands for t or q) through:

$$C_{x10} = \left[\frac{\kappa}{\ln(10/z_o) - \psi_m(10/L)} \right] \cdot \left[\frac{\kappa}{\ln(10/z_{ox}) - \psi_x(10/L)} \right] \tag{4}$$

In the Liu–Katsaros–Businger model (LKB; Liu et al. 1979), the scalar roughness length is parameterized in terms of the roughness Reynolds number, R_r , though:

$$z_{ox} = \frac{\nu}{u_*} f_x(R_r) \tag{5}$$

where ν is the kinematic viscosity of air and f_x is a polynomial function. LKB is an extension of Liu and Businger (1975) with eddies transporting heat between the bulk fluid and the sea surface through the interfacial layer (~ 1 mm depth) where molecular constraints on the transport are important.

The LKB method has been validated with field data for low wind speeds. Fairall et al. (2003) retained this interfacial scaling, yet they extended the parameterization for winds up to 18 ms^{-1} , based on a large amount of field data. In particular, they considered equal scalar roughness lengths, i.e. $z_{ot} = z_{oq} = \min(1.1 \times 10^{-4}, 5.5 \times 10^{-5} R_r^{-0.6})$. Andreas et al. (2008) have argued that the interfacial scaling should not be expanded in higher wind conditions ($U_{10} > 10 \text{ ms}^{-1}$) where sea spray has a significant influence on scalar fluxes.

According to Andreas et al. (2008, 2015), the sensible and latent heat fluxes H_s and H_L , respectively, are the sum of the interfacial and spray contributions (6) as the field measurements are taken above the droplet evaporation layer, which typically extends about one significant wave height amsl:

$$\begin{aligned} H_L &= H_{L,int} + H_{L,sp} \\ H_S &= H_{S,int} + H_{S,sp} \end{aligned} \tag{6}$$

with the subscripts *int* and *sp* referring to interfacial and spray contribution, respectively. $H_{L,int}$ and $H_{S,int}$ are parameterized based on LKB through the temperature and humidity roughness length using (5). Furthermore, $H_{S,sp}$ depends on the difference between the equilibrium temperature of spray droplets and the sea surface temperature (*SST*) while $H_{L,sp}$ depends on the mass lost by evaporation. Andreas et al. (2008) hypothesized that the microphysical behavior of droplets with initial radii of 50 μm and 100 μm , which contribute most of the $H_{L,sp}$ and $H_{S,sp}$, respectively, are representative diameter values for making the spray

flux estimation simpler and computational effective. It is important to note that Andreas' algorithm does not account explicitly for the spray particle production. Instead, it parameterizes spray-mediated fluxes through the microphysical behavior of 50 μm and 100 μm radius droplets and friction velocity. Microphysical quantities, such as e-folding time of temperature and radius for spray flux calculations are based on Andreas (2005). However, due to the complexity of the system and the difficulty to obtain direct observations, the extent to which sea spray facilitates air–sea transfer remains uncertain. Peng and Richter (2017, 2019) have investigated the underlying assumptions of sea spray bulk models through idealized direct numerical simulations in a Lagrangian–Eulerian framework. They found that the spray flux algorithm of Andreas et al. (2015) probably overestimates spray-mediated heat flux.

2.1 MIMICA LES model extended

MIMICA LES model (Savre et al. 2014) solves a set of anelastic, non-hydrostatic governing equations (Clark 1979) including momentum, ice/liquid potential temperature and total water mixing ratio on a Cartesian staggered Arakawa-C grid. The 2nd order Runge–Kutta time integration scheme is employed and the integration time step is calculated continuously to satisfy the Courant–Friedrichs–Lewy criterion. Momentum advection is performed using a 3rd order equation in conservative form. A quadratic upstream interpolation for convective kinematics type finite volume scheme is used to calculate scalar advection. A first order closure based on the turbulent kinetic energy (TKE) equation (Stull 1988) is used to estimate the subgrid scale TKE, e . Eddy diffusivity is modeled as $K_m = C_m l \sqrt{e}$, where C_m is a model constant and l is a characteristic turbulent length scale. The turbulent Prandtl number, Pr , is used to relate the momentum to the scalar eddy diffusivity as $K_h = K_m / Pr$. MIMICA takes into account a maximum of six classes of hydrometeors, and a two-moment bulk microphysics scheme (Seifert and Beheng 2001, 2006) is used to calculate the prognostic variables (mass mixing ratio, number concentration). A simple parameterization for cloud condensation nuclei (CCN) activation is applied (Khvorostyanov and Curry 2005), where the number of cloud droplets formed is a function of super-saturation and CCN concentration. In this study, grid points with condensed water q_c exceeding 0.001 g kg^{-1} are considered cloudy. The radiation solver of Fu and Liou (1993) considers the effects of the water vapor mixing ratio, cloud droplets and ice particles on radiation. The surface is treated as a solid wall with vertical velocity equal to zero with the following conventional surface boundary condition:

$$\tau_{i3,s} = \langle \tau_b \rangle \frac{\tilde{u}_i}{|\tilde{u}_r|} \quad (7)$$

where $\tau_{i3,s}$ is the instantaneous local (i.e. over an LES grid element) surface stress at each grid point ($i = 1, 2$ denotes the stream-wise and span-wise components); $|\tilde{u}_r| = \sqrt{\tilde{u}_1^2 + \tilde{u}_2^2}$ is the instantaneous resolved velocity magnitude at the first LES level (the \sim denotes LES resolved variable); $\langle \tau_b \rangle$ is the total stress calculated by a bulk air–sea flux algorithm in our study.

MIMICA has been expanded to include two bulk air–sea flux algorithms, COARE 3.5 (Edson et al. 2013) and Andreas' version 4.0 (Andreas et al. 2015). MOST provides ensemble-mean flux-gradient relationships in the surface layer. Nevertheless, MOST is commonly used in the LES approach in order to relate surface turbulent fluxes to resolved-scale variables (Albertson and Parlange 1999; Moeng 1984; Stoll and Porté-Agel 2006). Similarly, in this study the spatially averaged resolved wind velocity, air temperature, humidity and other atmospheric parameters at the first LES level are used as input parameters to both algorithms in order to estimate surface fluxes at each time step.

COARE 3.5 is an air–sea flux algorithm which estimates the momentum flux through C_{d10} by taking into consideration the momentum roughness length, gustiness, and atmospheric stability. The Charnock coefficient is obtained by the piecewise linear function of wind speed of Edson et al. (2013):

$$\alpha = 0.017U_{10m} - 0.005 \quad (8)$$

Further, this algorithm applies the empirical fit for z_{ox} of Fairall et al. (2003), as it was mentioned above.

Andreas' algorithm explicitly treats the interfacial and the spray-mediated fluxes. Both total heat fluxes (6) can be used as bottom boundary conditions to account for spray without considering the evaporation layer transfer mechanisms. The drag coefficient follows the work of Foreman and Emeis (2010), similar to the left hand side of Eq. (2) but with a constant added. The new parameterization is $u_* = C_m U + b$, where $\lim_{U \rightarrow \infty} C_d = C_m^2$ and b is a constant with dimensions of meters per second. The benefit of this method is that it produces a natural limit to the drag coefficient as the wind speed increases. This modification is necessary in hurricane models, as a simple extrapolation of the C_d from moderate to hurricane wind speeds underestimates the storm intensity.

2.2 Design of LES-CBLAST simulations

The simulated case is based on observations from the CBLAST-Hurricane experiment acquired during Hurricane

Isabel on September 12, 2003. The N43RF research aircraft flew low-level stepwise descents within the cold wake between rain bands at a distance of 100–150 km east of the storms' center. This aircraft collected HBL observations at 88–374 m amsl, which are suitable for estimation of heat and momentum flux as well as turbulence statistics (Drennan et al. 2007; French et al. 2007; Zhang 2007; Zhang et al. 2009; Zhang and Drennan 2012). In the vicinity of N43RF, the N42RF aircraft launched GPS dropsondes to measure the HBL vertical structure. The averaged profiles of wind speed, air temperature and humidity have been used for the model initialization (see Sect. 3.1.1).

In our study, the mesh resolution is chosen to be anisotropic and as fine as our computer resources permitted. Although higher resolution resolves smaller scales it showed little influence on the surface fluxes. The computational domain is a 512×512 grid in the horizontal plane with resolution set to $\delta x = \delta y = 10$ m. The vertical grid-spacing is $\delta z = 5$ m with a total of 300 layers. According to Berg et al. (2020), the LES grid-sensitivity issue persists down to a resolution of $\delta x = \delta y = 2.5$ m and $\delta z = 1.75$ m. Highly anisotropic grid spacing with coarse resolution suffices to reproduce the bulk cloud parameters (cloud fraction, liquid water path), but turbulence statistics are better reproduced as mesh resolution increases (Pedersen et al. 2016; Mellado et al. 2018).

Periodic lateral boundary conditions are used, and a sponge layer is defined in the vertical direction at the top 20% of the domain (from 1200 m to 1500 m). A constant SST of 300.18 K, and a surface pressure of 1002.9 hPa, derived from the observations, are used. The background (large-scale) vertical velocity is estimated using a horizontal wind divergence $D = -4 \times 10^{-6} \text{ s}^{-1}$, as it was determined from the ERA5 Global Reanalysis (Hersbach et al. 2020). For all simulations, the solar zenith angle, and hence the incoming solar energy, are kept constant in time at the observations local time (11:00 am). A constant surface albedo of 0.08 is considered across the domain and a value of the Coriolis parameter corresponding to the latitude $\varphi = 21.61^\circ \text{N}$. Assuming that the sea-spray particles which potentially act as CCN are already included, the CCN concentration is equal to 100 cm^{-3} . This is a typical value for marine air masses with no anthropogenic or continental effect (Allan et al. 2008; Wex et al. 2016). CCN are passively advected within the model domain and removed during droplet activation.

We performed three simulations with the CBLAST conditions, in order to examine the impact of sea spray on sensible and latent heat fluxes and their impact on turbulence statistics, MABL development and cloud properties. The first simulation (C) employs the COARE algorithm, which does not take into account the effect of sea spray. The

other two simulations use Andreas' algorithm; the original one (O) with the neutral drag coefficient estimated from Andreas' parameterization and a modified version (M) with a constant neutral drag coefficient ($C_{d10n} = 0.0015$) primarily for sensitivity testing. In order to avoid inaccurate spray fluxes in the M simulation, we employed the same spray-mediated heat transfer parameterization as in the O simulation. The reason for this is that the spray's transfer coefficients are estimated using the stress parameterization based on eddy-covariance measurements. Hence, whenever the stress parameterization is changed they need to be readjusted.

The simulations are compared using time-averages over the large eddy turnover time scale T_e , which is calculated by the ratio of Z_i (the boundary layer height) and the friction velocity scale u_* as $T_e \equiv Z_i/u_*$ (Berg et al. 2020; Moeng and Sullivan 1994). The boundary layer height Z_i is estimated every 30 s using the maximum gradient method (Sullivan et al. 1998) applied to the instantaneous horizontal-averaged virtual potential temperature θ_v , which accounts for both pressure and water vapor variations.

A non-nudging approach has been used for continuous turbulence development. The total simulation's duration is limited to ~ 5 h to avoid simulated profiles drifting further away from the initial CBLAST profiles. This would lead to a further reduction ($> 26\%$ for O simulation) of the near surface wind speed and the sea spray impact. Alternatively, a much higher gradient wind speed would be required to balance the frictional drag and prevent the surface wind from decreasing, which is unrealistic and computationally inefficient (Ma and Sun 2021). To address this issue and limit non-stationarity effects, a 2 h spin-up (~ 4 large eddy turnovers, i.e. $\sim 22,000$ time-steps) has been set with prescribed constant surface fluxes ($u_* = 0.4 \text{ ms}^{-1}$, $H_s = 5 \text{ Wm}^{-2}$, $H_L = 50 \text{ Wm}^{-2}$) lower than the prevailing ones. That allows turbulence and convection to develop within the domain before MIMICA starts to apply the surface fluxes through the bulk algorithms. The three simulations continued for ~ 3 h (~ 10 large-eddy turnovers, i.e. $\sim 70,000$ time-steps) after the spin-up and MABL reached a quasi-steady state. We define this quasi-steady state as the time when the variables of most interest in this study, i.e. the wind speed and momentum flux near surface, reach an equilibrium value.

The simulation results are averaged during the last large eddy turnover. In this study, the height of 10 m is used as reference height to estimate the LES surface turbulent fluxes, and the length scale z_o and the Obukhov length L are used to reduce the transfer coefficients to neutral stability. Table 1 shows the results of the averaged LES output and CBLAST data with a focus on fluxes and key meteorological

Table 1 N43RF mean values (French et al. 2007; Zhang 2007) and LES time-averaged values over $1T_e$ at the end of the simulation time

	N43RF CBLAST		Run C	Run O	Run M
	Mean (number of observations)	Standard deviation	Averaged values over all measurement heights (standard deviation)		
<i>Flight level height range 88–374m</i>					
$U(\text{ms}^{-1})$	29.9 (9)	3.5	25.2 (1.3)	25.8 (1.0)	26.7 (1.0)
$\theta(\text{K})$	301.2 (9)	0.2	301.078 (0.001)	301.395 (0.005)	301.406 (0.008)
$q(\text{g kg}^{-1})$	17.9 (9)	0.3	18.4 (0.1)	18.6 (0.2)	18.8 (0.2)
$ \tau/\rho ^{1/2}(\text{ms}^{-1})$	0.85 (9)	0.19	0.60 (0.03)	0.63 (0.03)	0.62 (0.02)
$\langle w'\theta' \rangle (\text{Kms}^{-1})$	-0.025 (7)	0.016	-0.0185 (0.001)	-0.0168 (0.001)	-0.0169 (0.001)
$\langle w'q' \rangle (\text{g kg}^{-1} \text{ms}^{-1})$	0.093 (8)	0.023	0.051 (0.003)	0.075 (0.003)	0.085 (0.003)
<i>Near surface 10m</i>					
$U_{10n}(\text{ms}^{-1})$	21.0 (9)	2.5	17.9	18.5	19.8
$\theta_{10n}(\text{K})$	301.5 (8)	0.3	300.8	301.2	301.2
$q_{10n}(\text{g kg}^{-1})$	19.2 (8)	0.4	19.2	19.5	19.9
$u_*(\text{ms}^{-1})$	0.92 (9)	0.18	0.65	0.70	0.68
$\langle w'\theta' \rangle_0 (\text{Kms}^{-1})$	-0.029 (7)	0.018	-0.017	-0.012	-0.012
$\langle w'q' \rangle_0 (\text{g kg}^{-1} \text{ms}^{-1})$	0.088 (8)	0.024	0.054	0.079	0.088

With the exception of U_{10n} , which is from the nadir-pointing stepped frequency microwave radiometer, the N43RF surface values are based on data extrapolation. COARE algorithm's profile functions $\psi(z/L)$ are used to reduce the LES data to neutral stability

parameters. Further analysis is provided in 3.1.1 and 3.1.2. It should be noted that the study focuses on a small region with hurricane-like conditions to investigate the impact of sea-spray fluxes under strong winds. A validation of the LES output against the available CBLAST flight measurements is not the scope of this study.

2.3 Spectral calculations

The initial velocity magnitude profile from CBLAST is aligned in the x direction, which has consequences for one-dimensional spectral properties (Berg et al. 2020). In this study the two-dimensional power spectral density from the LES is calculated using the fast Fourier transform method. The two wind components have been treated as scalar quantities assuming axisymmetric isotropy in the plane according to Kelly and Wyngaard (2006). Following Durran et al. (2017), the spectral density at $k_h = \sqrt{k_x^2 + k_y^2}$ is calculated using an integration around a ring of radius k_h centered at the origin of the wavenumber plane. The power spectral density of a variable integrated over k_h gives the variance. We use an ensemble average of the power spectral density derived by computing one spectrum per minute for 15 min and then temporal averaging.

3 Results

3.1 Observations and LES evaluation

3.1.1 Vertical structure

The CBLAST averaged profiles of wind speed U , potential temperature θ , water vapor mixing ratio q , virtual potential temperature θ_v , equivalent potential temperature θ_e , cloud water mixing ratio q_c , together with the available observed leg-averaged values and the corresponding LES profiles are shown at Fig. 1. The LES parameters are horizontally and temporally averaged for one large eddy turn-over interval ($T_e = 1425, 1487$ and 1584 s for C, O and M, respectively).

The potential temperature profile used for initialization is composed by a nearly constant θ layer below 500 m with a stable layer above it (Fig. 1b) (Zhang and Drennan 2012). This HBL structure is attributed to the moist processes in the wider storm area (latent heat release in clouds and rainfall evaporation below), as well as variations of radial advection of θ with height (Kepert et al. 2016). According to the dropsonde's averaged measurements the near surface atmosphere is warmer ($\theta_{10n} = 300.82$ K) than the SST (300.18 K). These observations are taken in the right rear quadrant of the storm, where intense ocean mixing causes sea surface cooling (Nolan et al. 2009). Furthermore, the initial equivalent potential temperature, θ_e , a conserved variable in dry and moist

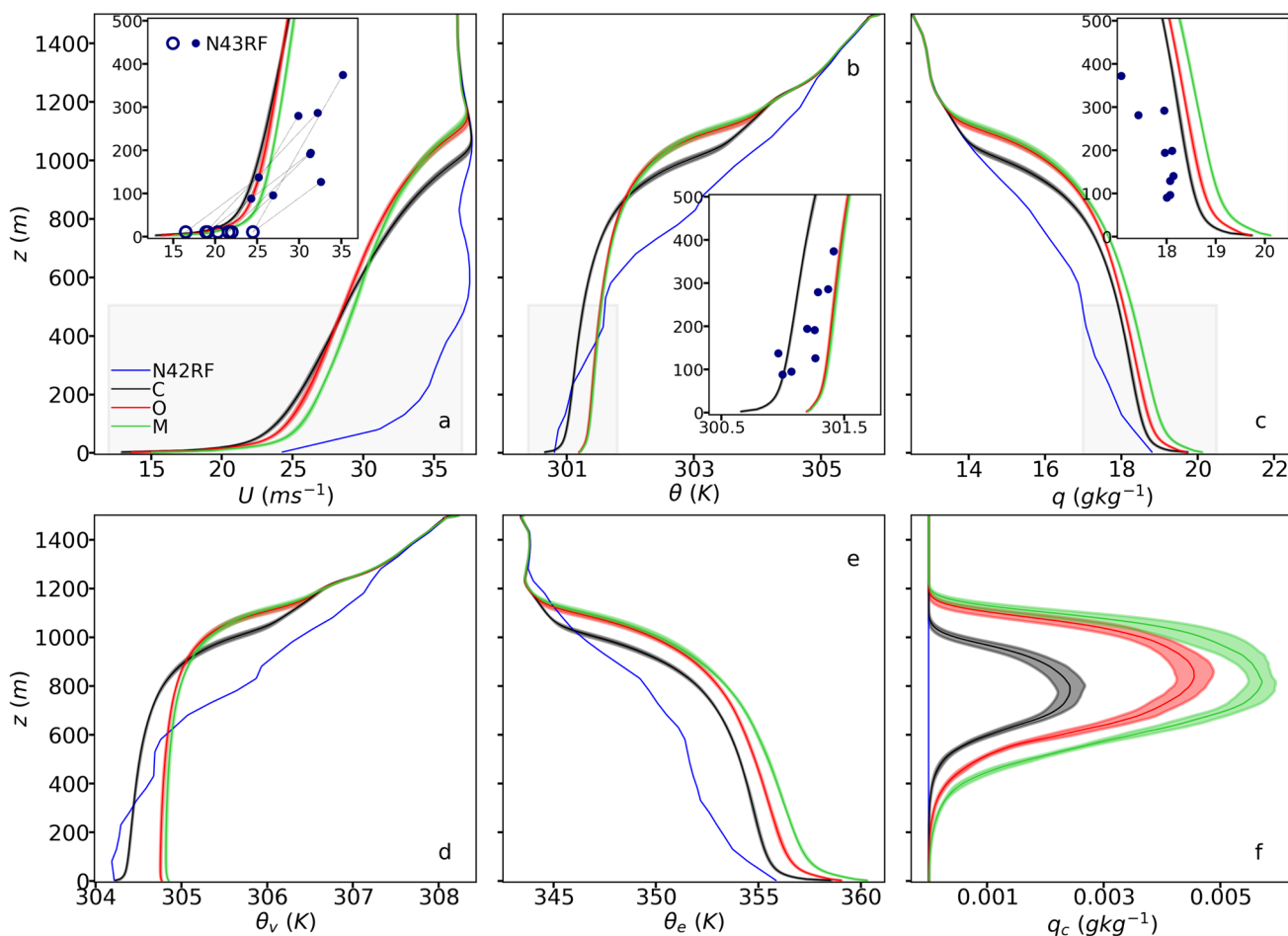


Fig. 1 Horizontally and temporally averaged (time averaging is done for $1T_c$) profile of **a** wind speed U ; **b** potential temperature θ ; **c** water vapor mixing ratio q ; **d** virtual potential temperature θ_v ; **e** equivalent potential temperature θ_e ; **f** cloud water mixing ratio q_c . The shaded profiles areas indicate the standard deviation of the profiles, blue line

indicates the N42RF averaged CBLAST profile during Hurricane Isabel on September 12, 2003 (Zhang and Drennan 2012), closed blue circles represent flight leg-averaged values taken by N43RF at 374, 286, 279, 194, 191, 137, 126, 95, 88 m height, and open circles are the corresponding near-surface values (French et al. 2007)

adiabatic processes without precipitation, indicates moist convective instability, as it decreases with height (Fig. 1e). The equivalent potential temperature has been calculated using Bolton (1980) formula; $\theta_e = T \left(\frac{1000}{P} \right)^{0.2854(1-0.28 \times 10^{-3} q)}$ $\exp \left[\left(\frac{3.376}{T_L} - 0.00254 \right) (1 + 0.81 \times 10^{-3} q) \right]$, where T, P, q are the absolute temperature, pressure and water vapor mixing ratio at the initial level, respectively, and T_L is the absolute temperature at the lifting condensation level.

The LES profiles evolved as the simulations progressed, resulting in a much deeper and better mixed layer than the initial one as evidenced by the vertical distributions of u, θ, q, θ_v and θ_e (Fig. 1). This is consistent with previous LES studies conducted under conditions of severe winds and moderate air–sea heat fluxes, in which the boundary layer grows beyond 1km depth as the inversion is eroded by the strong winds (Bryan et al. 2017; Chen et al. 2021;

Green and Zhang 2015). According to Chen et al. (2021), if the term of rotation and associated centrifugal acceleration were included in the simulations, the boundary layers would have been shallower. The three simulations estimate average wind speed in the interval of 25.2–26.7 ms^{-1} (Table 1) at the layer of aircraft measurements, albeit they are within the low-end range of the N43RF leg-averaged wind speed values (24.3–35.2 ms^{-1} , Fig. 1a). Correspondingly, the simulated U_{10n} values (17.9–19.8 ms^{-1}) are at the lower-end range of the observed near surface wind speed values (16.5–24.5 ms^{-1}). It is also interesting to mention that the near surface LES wind speed profiles deviate from the logarithmic law by up to -21% , -18% and -16% for C, O, and M, respectively. There is also a step-like decrease of the fluxes below 10 m (Fig. 2a–c), indicating that the near-surface flow is poorly resolved (Maronga et al. 2020). Simulation C forms the coldest, driest, and shallowest MABL (1012 m), while O and M

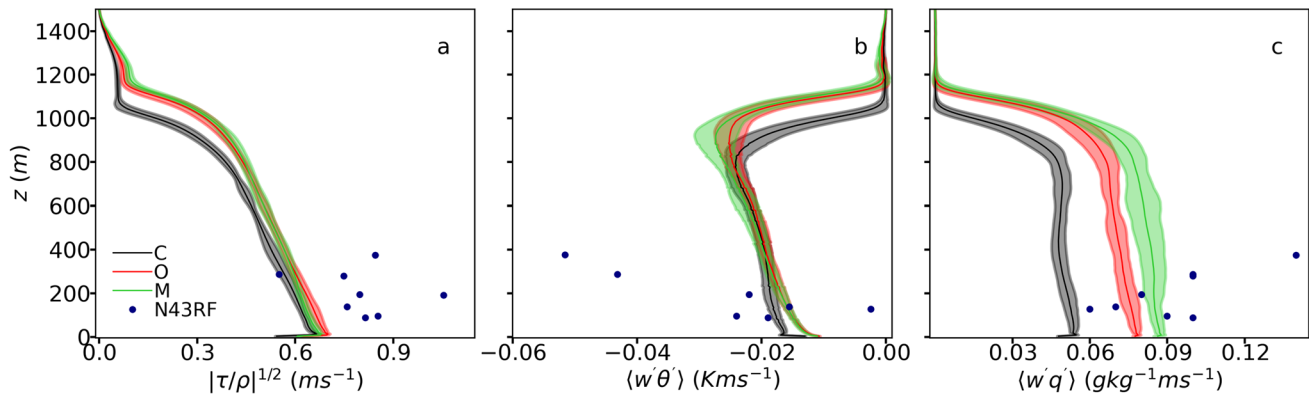


Fig. 2 Time-averaged (T_e) profile of **a** stress covariance $|\tau/\rho|^{1/2}$; **b** vertical velocity and potential temperature covariance $w'\theta'$; **c** vertical velocity and water vapor mixing ratio covariance $w'q'$. The shaded

profiles areas indicate the standard deviation of the profiles, and blue circles represent leg-averaged values taken by N43RF (French et al. 2007; Zhang et al 2008)

develop warmer and more humid layers of 1109 m and 1120 m height, respectively. Regarding the temperature values, those from O and M simulations are found to be higher than the observed ones, whereas those from C are in the lower range (Fig. 1b). This is due to the heat flux spray-mediated contribution as well as the higher heat budget caused by the enhanced entrainment of warmer air from aloft. The entrainment rates $w_e = dZ_i/dt + DZ_i$, which have been determined according to Bretherton and Wyant (1997) and averaged throughout the simulations, have values of 0.034, 0.043 and 0.044 ms^{-1} for C, O and M, respectively.

The sea-surface water vapor mixing ratio is estimated to be $\sim 23 \text{ g kg}^{-1}$ (with 98% saturation), resulting in a 4.25 g kg^{-1} initial air–sea difference. As a result, all simulations produce a moister layer than the observations, with O and M accumulating more water vapor than C due to spray-mediated contribution to the moisture flux (Fig. 1c). Shpund et al. (2012) found that when the relative humidity (RH) is low ($< 90\%$), the sea spray evaporation moistens and cools the boundary layer, which is consistent with our simulations where the near surface RH is less than 85%. The moist conditions, aided by the conditional instability (i.e. negative θ_e and positive θ gradient at the same time), contribute to the development of a cloud layer (no drizzle is detected) in all simulations, although the initial cloud water mixing ratio, q_c , is zero. The mean cloud liquid water path (LWP) for C, O and M, however, is small at 0.95, 2.4 and 3.3 gm^{-2} , despite a cloud layer depth of 228, 453 and 561 m, respectively (see Sect. 3.3). The difference in the amount of condensed water accumulated between simulations M and O is due to the larger contribution of the spray component to the moisture flux in simulation M (see Sect. 3.1.2), as the entrainment and θ structure of these simulations is nearly identical.

3.1.2 Fluxes

The surface momentum flux changes abruptly when the algorithms are employed after spin up, with u_* more than doubling its prescribed value, which is analogous to airflow encountering a new roughness zone (from smooth to rough). Due to the strong feedback between the momentum flux and the near surface wind speed, the wind velocity decreases exponentially during the early stages of the simulations, with C and M having the highest and lowest reductions, respectively, due to the different stress parameterizations. During that time-frame, the vertically integrated TKE grows linearly with time in response to the change in surface fluxes before flattening (not shown). The reduction of u_* and U_{10m} during the averaging T_e is less than 2.3% and 2%, respectively. Accordingly, the vertical momentum and heat fluxes distribution initially exhibit a high rate of change with height, gradually decreasing as the boundary layer evolves toward a quasi-steady state (not shown).

Figure 2a–c displays the time-averaged profiles of stress $|\tau/\rho|^{1/2}$, kinematic sensible heat $\langle w'\theta' \rangle$ and moisture $\langle w'q' \rangle$ flux at the final stage of the simulation period, as well as the N43RF observed flux values. The averaged fluxes show a linear change with height from their surface values to their respective entrainment values in agreement with theory (Wyngaard 1992). Furthermore, the LES Reynolds stress varies slightly between the simulations (0.60–0.63 ms^{-1}) and is at the low end of the observed range (0.55–1.26 ms^{-1} , Fig. 2a). However, the scatter of the measurements, due to measurements errors (sampling errors, correlation time lag errors, deviations of the aircraft altitude etc.), prohibits an explicit conclusion about the stress behavior at or near hurricane wind speeds (French et al. 2007; Drennan et al. 2007). Richter and Wainwright (2023) also report minor differences of the surface stress between spray-laden and unladen simulations in an LES framework which explicitly took sea spray

particles into account. According to our simulations, stress increases from the aircraft level (88 and 374 m) to the surface by 3% and 17%, while the height-based correction of the observed stress to the surface is 10%–15% (French et al. 2007).

A small downward surface sensible heat flux, which increases with height up to the middle of the cloud layer, is apparent in all simulations (Fig. 2b). The heat flux profile derived from the best fit line of the observations shows the same trend (Zhang et al. 2008). The air–sea temperature difference in simulation C is the smallest of the three, whereas its surface downward $\langle w'\theta' \rangle$ is the highest (Table 1). Within the evaporation layer, the spray-mediated sensible heat flux, which is considered by the Andreas' algorithm in simulations O and M, has positive values of 0.012 and 0.015 Kms^{-1} and compensates for the negative interfacial heat flux (-0.023 and -0.026Kms^{-1} , respectively). The spray-mediated sensible heat flux is caused by two processes: the cooling of the saline spray droplets to obtain thermal equilibrium with the environment releasing sensible heat (Andreas 1995), and the evaporation of sea spray droplets consuming sensible heat (Andreas et al. 2008). Thermal equilibrium is reached when the sea spray droplets attain temperatures close to the wet-bulb temperature ($\sim 298.4 \text{K}$) which is much lower than the air temperature at 10 m height.

For all simulations, the moisture flux vertical distribution is roughly constant with height up to the cloud base (Fig. 2c). Likewise, the measured best fit moisture flux profile is nearly constant with height (Drennan et al. 2007). While O and M are found to be near the middle of the observed range ($0.052\text{--}0.136 \text{g kg}^{-1}\text{ms}^{-1}$), the moisture flux of C is slightly below due to the absence of the spray-mediated contribution. According to Andreas et al. (2015), the large spray heat fluxes typically correspond to near-neutral conditions with strong winds ($|z/L| \rightarrow 0$), where z is the measurement height. Since L is proportional to u_*^3 , the spray contribution is expected to be considerable for these conditions (i.e. near-neutral stability, high air temperature and strong winds) as $H_{L,sp}$ scales according to $u_*^{2.39}$ and the droplet's evaporation rate increases exponentially with ambient temperature. Within the evaporation layer, the spray-mediated component of the moisture flux is, 0.026 and 0.038 $\text{g kg}^{-1}\text{ms}^{-1}$ for simulation O and M as the RH is low, which is consistent with Shpund et al. (2012). The interfacial component is 0.052 and 0.049 $\text{g kg}^{-1}\text{ms}^{-1}$, respectively. The difference in wind velocity ($\Delta U_{10m} = 1.3 \text{ms}^{-1}$) is the main factor behind the discrepancy in $H_{L,sp}$ between O and M rather than the difference in water vapor ($\Delta q_{10m} = 0.4 \text{g kg}^{-1}$) or RH. Evaporation of spray droplets is also greater for M, due to the droplets longer residence time in the air under higher by 0.6 m significant wave height conditions (which is proportional to U_{10m} , according to Andreas and Wang 2007).

The surface virtual potential temperature flux, which is defined as $\langle w'\theta'_v \rangle = \langle w'\theta' \rangle(1 + 0.61q) + 0.61\theta\langle w'q' \rangle$, is initially positive in the O and M simulations, but evolves into a downward flux due to the considerable reduction of the spray flux towards equilibrium. In contrast, it is always downward in the C simulation which excludes spray contribution. Richter and Wainwright (2023) have reported that sea spray fluxes can modify the total fluxes under particular conditions as the excess of spray heat fluxes saturates the nearby surface layer and brings temperature and humidity values back into equilibrium. As a result, during the averaging T_e time period, the stability parameter $-Z_i/L$ has similar values in all three simulations (-0.45 , -0.35 , and -0.38 for C, O, and M, respectively), which indicates near neutral conditions with negative buoyancy flux. This is consistent with the observational study of Zhang et al. (2008) and Zhang (2010) who found slightly stable conditions above the cold wake of Hurricane Isabel in the right rear quadrant. It should be noted that Barr et al. (2023) reproduced the cold wake in a coupled numerical study, which was a major source of variability of near surface thermodynamics when compared to the other storm quadrants.

3.2 Turbulence

3.2.1 Flow visualization

Visualization of the instantaneous turbulent quantities $x' = x - \bar{x}$, where x is the instantaneous resolved quantity and \bar{x} the instantaneous horizontal average at a specific level, are shown in Figs. 3, 4, 5 and 6. The selected flow fields of the residual resolved stream-wise velocity (x -axis) u' , vertical velocity component w' , potential temperature θ' and water vapor mixing ratio q' , in the x - y ($z = 0.2 Z_i$) and z - y ($x = 2500 \text{m}$) planes are instantaneous snapshots obtained in the final stage of the simulation.

Coherent streaky structures are closely aligned with the mean flow direction in simulation C (Fig. 3a). These elongated high and low-speed agglomerations are visible in Fig. 3d in the bulk of the layer ($z < 0.9 Z_i$). However, since they are related to shear (Lee et al. 1990) they become more cellular, lose intensity, and rotate in relation to the mean flow with increasing height (Fig. 10). They are the primary coherent features of sheared boundary layers (Robinson 1991), which have been reported in both numerical and observational hurricane boundary layer studies (Lorsolo et al. 2008; Chen et al. 2021).

The small horizontal streaks found in C are arranged into larger scale structures in simulations O and M (Fig. 3b, c) as a result of the combined effects of shear and enhanced latent heat flux. Figure 3c shows a well-defined structure with its axis parallel to the mean flow, spanning the entire domain lengthwise with a high-speed

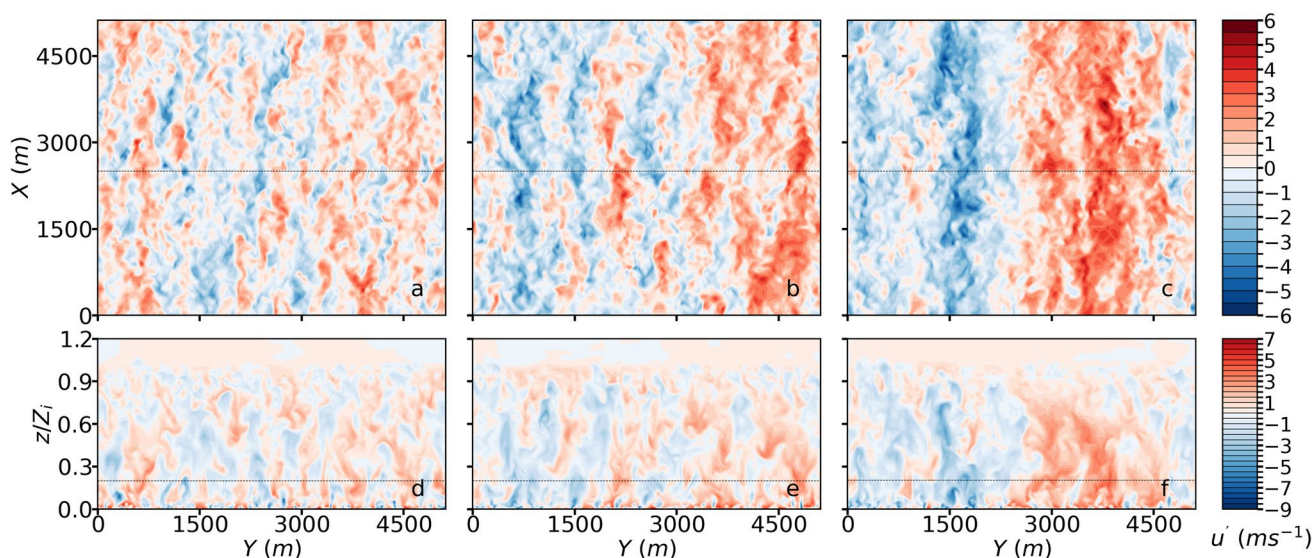


Fig. 3 Contours of the instantaneous residual stream-wise velocity u' ; 1st row, at $0.2 Z_i$ in the x - y plane for simulation **a** C; **b** O; **c** M; 2nd row, the same as the 1st row but for the z - y plane ($x = 2500$ m)

the height is normalized by Z_i . The dashed lines in **a**, **b** and **c** figures indicate the position of the cross sections shown in **d**, **e** and **f** figures, respectively, and vice versa

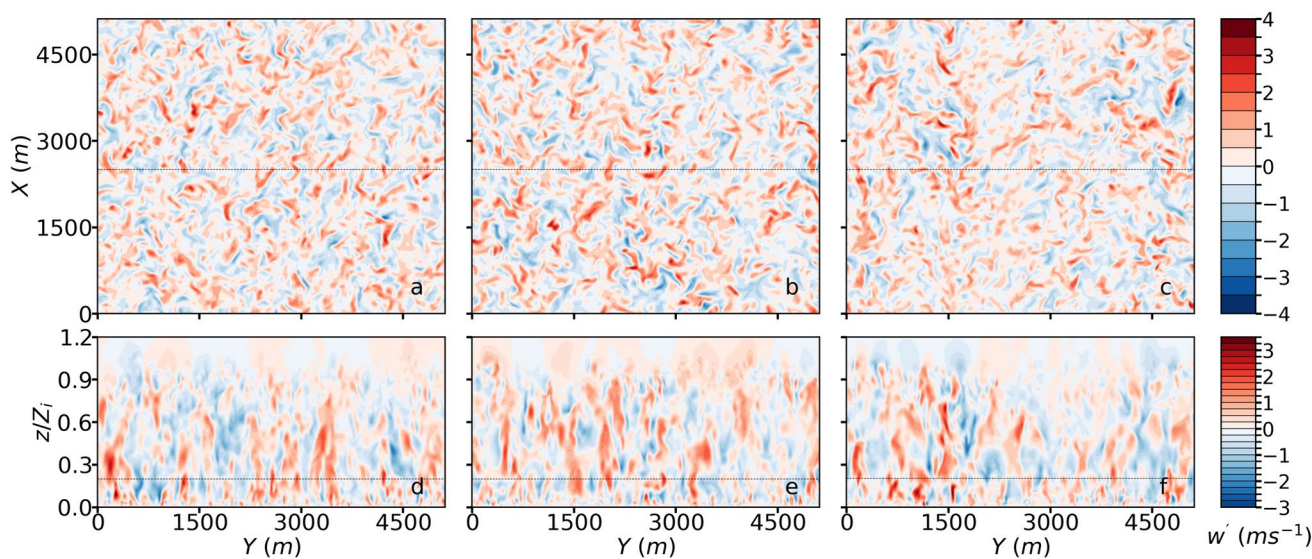


Fig. 4 Same as in Fig. 3, but for the instantaneous residual vertical velocity w'

region width of around $1.5 Z_i$. This structure is not spatially stationary in time and it is shifting to the left in relation to the x -axis. The results from simulation O lie between the other two simulations; the streaks are wider than in simulation C and the u' structure is less organized than in simulation M (Fig. 3b). This is also demonstrated by the magnitudes of the spectral density at the larger resolvable scales (Fig. 11). The structures lose coherence as height increases, yet they can be identified up to $\sim 0.5 Z_i$ for O and $\sim 0.7 Z_i$ for M (Fig. 3e, f). A visual inspection of the u' , θ' and q' fields (Figs. 3, 5 and 6) shows that the

lower-speed regions ($u' < 0$) are strongly correlated with the moister ($q' > 0$) and colder ones ($\theta' < 0$) due to the upward moisture flux as well as the downward heat flux. An opposite correlation was found between u' and θ' variations by Khanna and Brasseur (1998) under near-neutral conditions but with an upward temperature flux. The correlation coefficient, which is defined as $\gamma_{x,y} = \langle x'y' \rangle / \langle x'^2 \rangle \langle y'^2 \rangle$, is high near the surface ($\gamma_{u,\theta} \approx +0.85$ and $\gamma_{u,q} \approx -0.85$) for all simulations, and decreases rapidly with height up to the middle of the layer for simulation C. For simulation M it remains strong up to the middle of the layer, likely due to

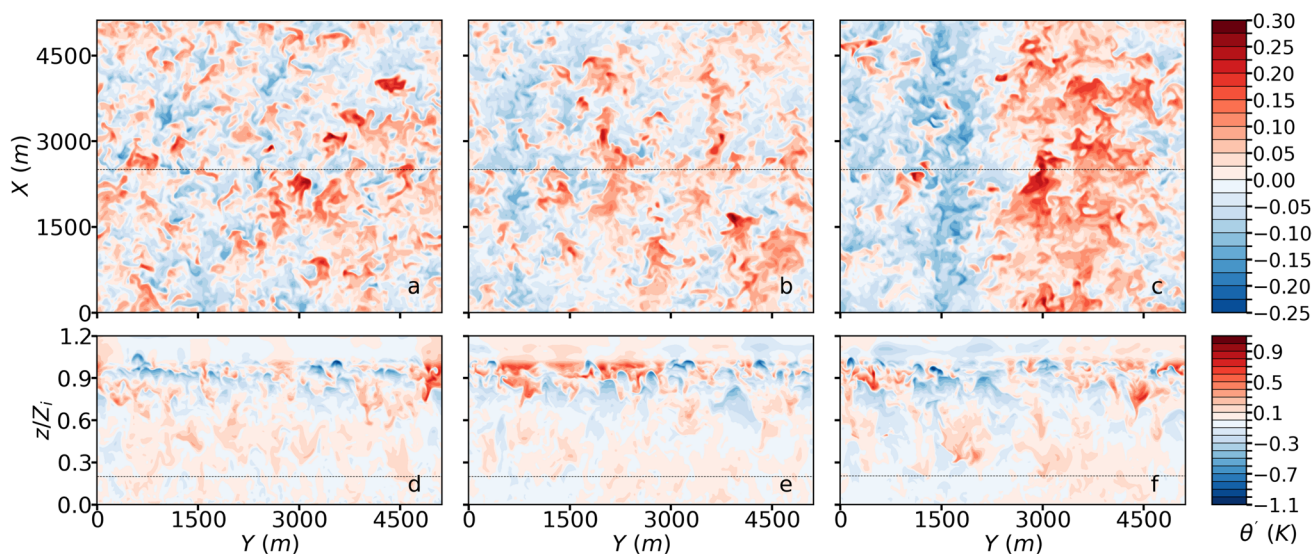


Fig. 5 Same as in Fig. 3, but for the instantaneous residual potential temperature θ'

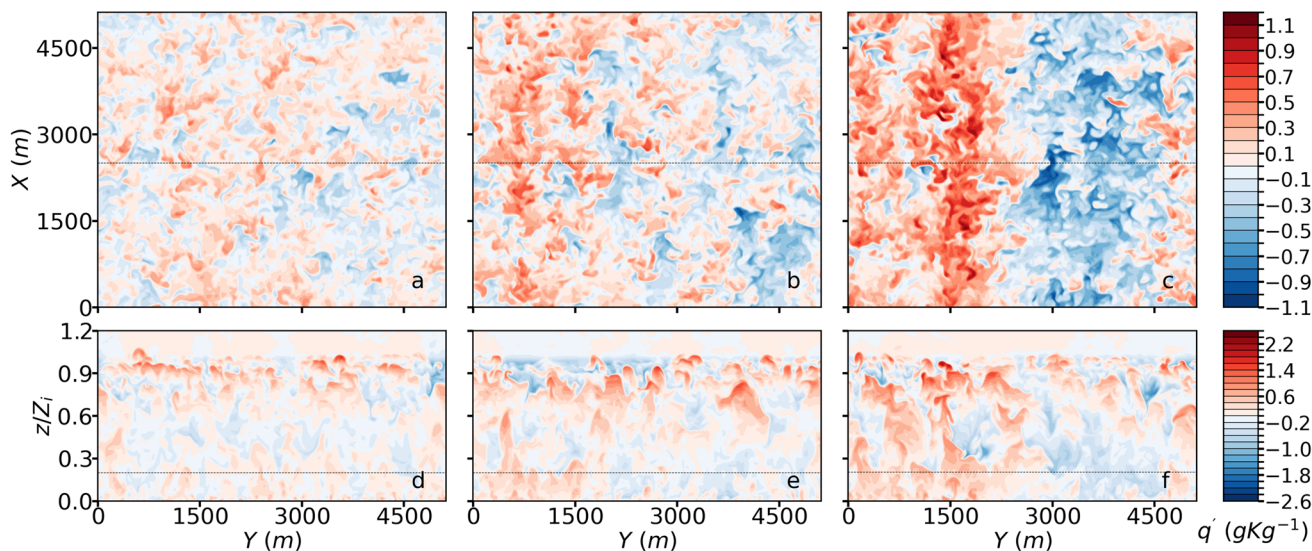


Fig. 6 Same as in Fig. 3, but for the instantaneous residual water vapor mixing ratio q'

the stronger scalar fluxes and the presence of the coherent u' structure (Fig. 12). The correlation coefficient for simulation O is found between the other two. The increased correlation values just below Z_i show that the temperature inversion plays a similar role in the organization of streaks as a boundary (lid) like a surface does. A similar effect has been seen in LES simulations (Moeng and Rotunno 1990) for the skewness of vertical velocity near Z_i , and it was attributed to change of eddy shape due to the presence of the inversion. However, this was generally not seen in the observations (Moyer and Young 1991).

Near the surface, streaky small plumes are found in all simulations with comparable structures, which is also evidenced by their spectra (not shown). These streaky small plumes merge with the nearby ones as they rise, and become organized into larger elongated updrafts (shifting the spectral peak towards lower frequencies) with increased vertical velocities (Fig. 4). The buoyancy forces within the large coherent u' structures, where the scalars (moisture and temperature) are concentrated, are negligible ($-0.4 < -Z_i/L < -0.3$). Hence they do not greatly differentiate the vertical velocity structure of O and M simulations with regard to C. This structure is in contrast

to the one reported by Khanna and Brasseur (1998) and Moeng and Sullivan (1994) on moderately convective sheared boundary layers, but buoyant enough to drive large coherent sheet-like updrafts. Despite the fact that the typical vertical structure is streaky throughout the MABL in all simulations, M appears to produce wider scale vertical motions above mid-MABL, as the elongated updrafts appear to be suppressed/enhanced above the high/low speed (u') region (Fig. 13c). This is corroborated by the fact that the spectral density in M is higher than the other two simulations at large resolvable scales (not shown).

3.2.2 Variances

The time-averaged variance profiles of the resolved wind speed components, potential temperature and water vapor mixing ratio, normalized by the surface layer scaling parameters (u_* , θ_* and q_*), are presented in Fig. 7.

The variance of the horizontal velocity components takes its maximum value near the surface ($z < 0.05 Z_i$) due to wind shear and decreases with height (Fig. 7a, b). Similar non-dimensional variance profiles have been reported by Chen et al. (2021) and Nakanishi and Niino (2012). The peak variance of the cross-stream velocity is lower than the value of the stream-wise component since the initial velocity profile is considered to align in the x direction. In particular, the peak values of u'^2/u_*^2 and v'^2/u_*^2 profiles in simulations C, O and M, are 16.5, 17.5 and 19 and 3.7, 2.7 and 2.5, respectively. Simulation C shows the highest cross-stream variance, due to increased wind rotation induced by the frictional drag (not shown). Further, simulation M has a higher stream-wise velocity variance than the other two simulations up to $0.6 Z_i$, which enhances the corresponding profile of turbulent kinetic energy (not shown). The vertical velocity variance w'^2/u_*^2 profile peaks (~ 1.20) at a higher level ($\sim 0.15 Z_i$) for all simulations (Fig. 7c), which is consistent with the Monin–Obukhov scaling functions

$w'^2/u_*^2 = 1.25(1 + 0.2z/L)$ for near-neutral conditions according to Högström (1988).

Because of entrainment processes, the most intense fluctuations, as demonstrated by the visualization of the turbulent flow fields θ' and q' (Fig. 5 and 6), occur around Z_i . Hence, both variance profiles peak at this height for all simulations (Fig. 7d, e). Although simulation C has the lowest q'^2 (not shown), it has the highest q'^2/q_*^2 peak value due to the lower surface moisture flux compared to O and M (Fig. 7e). In all simulations, the temperature and water vapor variances decrease with height and become nearly constant below $0.2 Z_i$ and $0.7 Z_i$, respectively, reaching their lowest values near the surface. It should be noted that in simulation M similarly to the variance of the stream-wise velocity, the variances of potential temperature and water vapor mixing ratio have their largest values in the mixed layer compared to the other simulations. This is due to the convergence of warmer/moister air within the higher/lower speed zones of u' coherent structure in simulation M.

The vertical velocity skewness $\langle w'^3 \rangle / \langle w'^2 \rangle^{3/2}$ represents the symmetry in the turbulence structure. The nearly steady positive value inside the MABL (Fig. 14a), similarly to observations in stratocumulus cloud (Lenschow et al. 1980; Moyer and Young 1991), suggests that updrafts are narrower/stronger than downdrafts. At the upper portion of the temperature inversion, vertical velocity skewness turns negative, which indicates that downdrafts are narrower and more intense than the updrafts. The negative temperature and positive humidity skewness suggest that downdrafts are dominated by colder and moister air (Fig. 14b, c). These negatively buoyant downdrafts may be produced by a small radiative cooling at cloud top (Fig. 14d). However, part of these downdrafts may be due to the head of folding thermal plumes, which have reached the MABL top from below and then they descend, leading to engulfment of warmer and drier air.

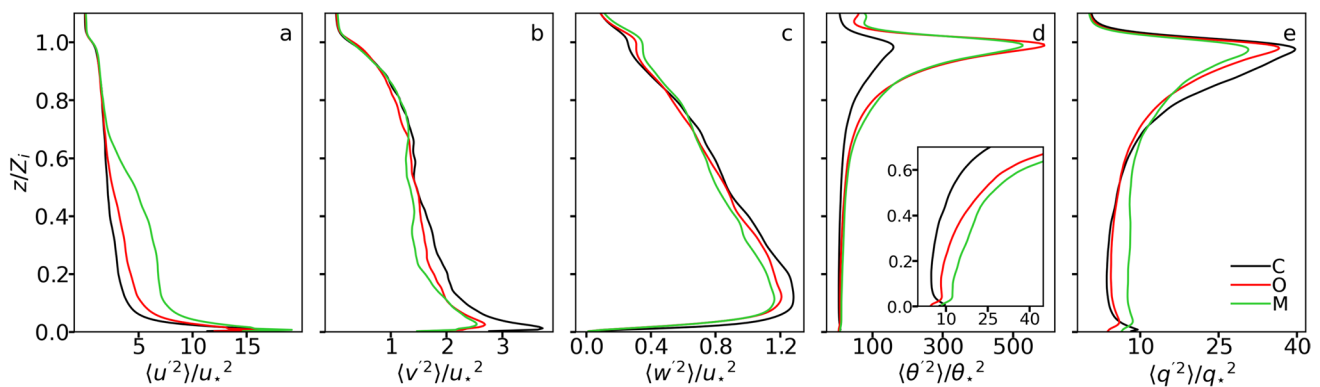


Fig. 7 Horizontally and temporally averaged (time averaging is done for $1T_e$) normalized variance profiles of the resolved **a** stream-wise; **b** span-wise; **c** vertical component of wind speed; **d** potential temperature and **e** water vapor mixing ratio

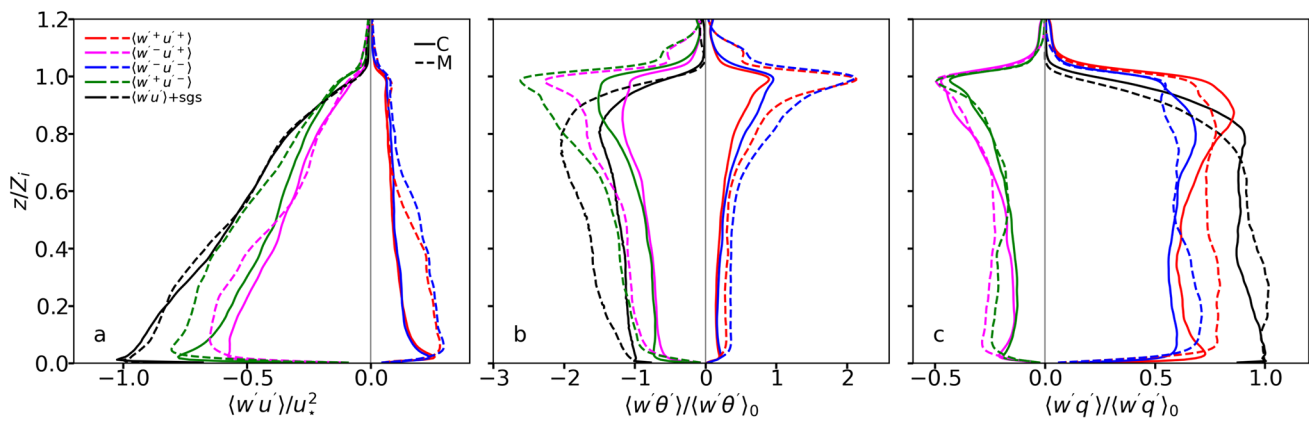


Fig. 8 **a** Temporally averaged vertical profiles of quadrant component momentum fluxes normalized by the surface flux for simulation C (solid lines) and M (dashed lines); **b** the same as (a) but for heat flux; **c** the same as (a) but for moisture flux

3.2.3 Quadrant analysis

A quadrant analysis of momentum, heat, and water vapor fluxes (Mahrt and Paumier 1984; Sullivan et al. 1998) is carried out to determine the differences found between simulations C and M (Fig. 8).

The lack of an entrainment peak in the momentum fluxes indicates the negligible net momentum transfer from the free atmosphere to the boundary layer (Fig. 8a). Up to the height of $0.6 Z_i$ where the u' structure loses coherence, each component of M is larger than its corresponding component of C in absolute magnitude due to the increased turbulent kinetic energy. Above this level, only the difference between their outward interactions ($w' > 0, u' < 0$) remains noteworthy. However, the profile of total flux in both simulations is similar and peaks at the surface due to drag (Fig. 8a). Furthermore, the ejections ($w' > 0, u' > 0$) and sweeps ($w' < 0, u' < 0$) are roughly equal for both simulations, whereas the outward interactions are stronger than the inward ones ($w' < 0, u' > 0$).

The maximum total downward heat flux for both simulations is located at a height of about $0.8 Z_i$, as it is shown in Fig. 8b. The peak magnitude of the individual quadrant fluxes is found near Z_i , where the potential temperature gradient is steepest and the corresponding fluctuations are most pronounced. The quadrant heat fluxes are largely self-canceling around Z_i , and even though air is exchanged between the boundary layer and the free atmosphere, as the large individual quadrant fluxes show, there is no considerable net vertical heat transfer. Maronga and Li (2022) argued that gravity waves at the top of the boundary layer are responsible for strong quadrant component values and at the same time for absence of a pronounced net heat transport. In both simulations, cooler air moving upward contributes the most to the total heat flux followed by warmer air moving downward,

with the other two components ($w'\theta' > 0$) contributing similarly (Fig. 8b).

Since the moisture supply is from below, the net moisture flux is upward, and the maximum flux in both simulations is at the surface (Fig. 8c). The peak magnitude of the outward and inward interactions ($w'q' < 0$; Fig. 8c) appears near Z_i , for both simulations. The MABL of M simulation is well-mixed and, thus, the ejections and sweeps ($w'q' > 0$) are roughly constant with height. In contrast, there are two peaks in the C simulation, one stronger in the region of $0.8\text{--}0.9 Z_i$ and the other one near the surface. The dominant eddy type contributing to the total profile is moist air moving upwards, followed by dry air moving downward. Similar to momentum, the magnitude of each individual component in M, especially the upward ones, appears to be strengthened in comparison to C simulation below $0.6 Z_i$, which results in a slightly greater net moisture transport in this regime (Fig. 8c).

3.3 Clouds and radiation

In this section the thermodynamic impact of sea-spray on cloud formation is examined. Large eddies can transport spray droplets upward, changing the thermodynamic structure of the mixed layer and forming clouds by condensation and collisions (Shpund et al. 2012, 2014). Note that investigation of the role of sea-spray as CCN is beyond the scope of this study and, thus, all simulations are performed with the same CCN conditions (see Sect. 2).

Simulation C produces scattered cloud structures (Fig. 9a), while simulations O and M, which are characterized by larger surface moist fluxes (Fig. 2c), produce an extensive cloud deck throughout the domain (Fig. 9b, c). In all simulations, the modeled cloud tops are confined by the MABL top, which is a typical structure of marine stratocumulus (Fig. 15). Thus, the development of the MABL

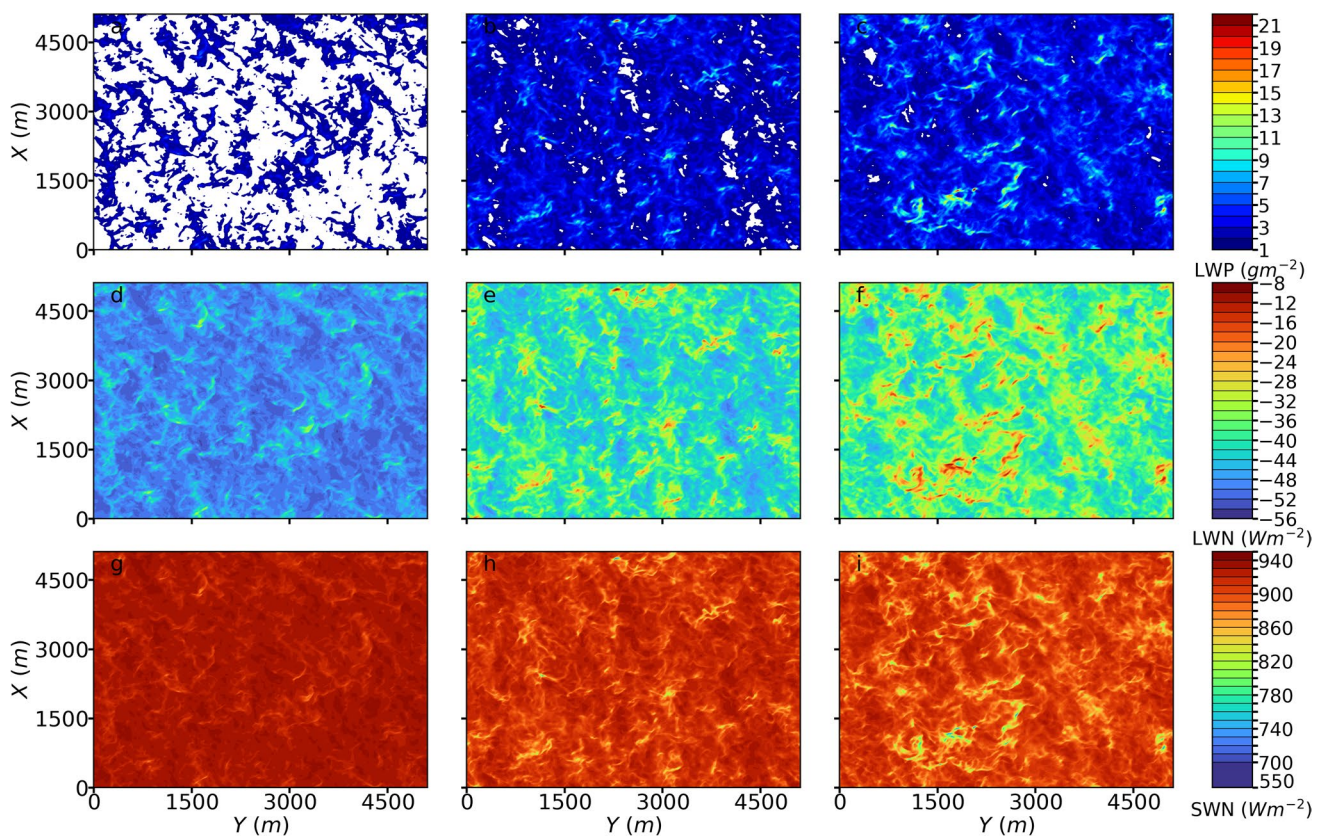


Fig. 9 1st row, contours of the instantaneous liquid water path for simulation **a** C; **b** O; **c** M; 2nd row, the same as the 1st row but for the surface long-wave net radiative flux; 3rd row, the same as the 1st row but for the surface short-wave net radiative flux

is critical to cloud formation, growth and accumulation of liquid water. However, in the present study the development of the MABL may not be realistic due to the lack of consideration for storm-scale dynamics.

LWP values are very low, usually below 5 gm^{-2} (8 gm^{-2}) in C (O and M) simulations. Local LWP maxima do not exceed 22 gm^{-2} in any simulation, with the largest values found in M (Fig. 9c). These differences in cloud liquid properties result in differences in the surface net long-wave (LWN) and short-wave radiation fluxes (SWN). The near cloud-free condition in simulation C is generally characterized by LWN values between -40 and -56 Wm^{-2} (Fig. 9d). As clouds develop in simulations M and O, they affect the surface LWN balance by emitting long-wave radiation downwards, which partially offsets the surface long-wave cooling. LWN values correlate with differences in LWP, with higher liquid amount resulting in increased LWN. In particular, clouds with LWPs $< 8 \text{ gm}^{-2}$ usually correspond to LWNs between -45 and -30 Wm^{-2} , while optically thicker cloud structures with LWPs $> 10 \text{ gm}^{-2}$ (mostly found in M simulation) can increase surface

LWN up to -10 Wm^{-2} (Fig. 9c, f). SWN in simulation C varies between 890 and 950 Wm^{-2} (Fig. 9g). As clouds form in simulations O and M, they reflect the incoming solar radiation reducing SWN locally (Fig. 9h, i). When LWP exceeds 8 gm^{-2} , changes in the surface shortwave budget become very prominent with SWN values falling below 850 Wm^{-2} . Overall, the mean surface net radiative fluxes (LWN + SWN) for C, O, and M are 870 , 855 and 840 Wm^{-2} , respectively, which indicates that changes in the air–sea flux treatment can alter the surface radiation budget by 30 Wm^{-2} through modifications in the cloud field.

4 Conclusions

In this study, the air–sea interaction mechanism has been incorporated into MIMICA LES code to study the MABL structure and cloud macro-physical properties under severe

wind conditions. The air–sea interaction mechanism is implemented into the LES code via two bulk air–sea flux algorithms: Andreas' algorithm which explicitly account for the interfacial and the spray-mediated fluxes and COARE algorithm. Three high resolution simulations have been performed using the COARE algorithm (simulation C), the original Andreas algorithm (O) and a modified version (M) which reduces the shear stress and increases the scalar fluxes for the same wind speed compared to O.

The profiles used for model initialization are from the CBLAST-Hurricane campaign, which acquired turbulence flux data from Hurricane Isabel within the storm's cold wake on September 12, 2003. Measurements demonstrate friction velocity values with substantial scatter ($0.55\text{--}1.26\text{ ms}^{-1}$), strong moisture fluxes ($0.052\text{--}0.136\text{ g kg}^{-1}\text{ ms}^{-1}$), and the sensible heat fluxes in the stable to near neutral regime ($-0.05\text{ to }-0.0023\text{ Km s}^{-1}$).

All simulations produce a deeper well mixed layer and a decrease in wind speed values compared to the initial profiles. The values of the near-surface wind speed and the momentum flux are at the low end of the observed range and they differ only slightly between simulations. Sea spray fluxes decrease as the simulations proceed, primarily due to a decrease in near-surface wind speed and, secondarily, due to changes in near-surface thermodynamic conditions. To sustain large spray fluxes, a mechanism should be incorporated such as advection, strong updrafts or water phase transition which could effectively remove moisture and heat from the surface layer and prevent saturation by the enhanced fluxes (Richter and Wainwright 2023).

Spray-mediated sensible heat flux is opposite to the interfacial flux and accounts for up to 60% of its magnitude. Thus, sea spray distinguishes the O and M simulations thermodynamically by increasing the potential temperature profiles compared to C. This is mainly due to the increased TKE production when spray is considered, which promotes MABL growth and entrainment of warmer air from aloft. In all simulations, the total sensible heat flux is downward, (but there is conditional convective instability) which is less than the observed mean but within the observed range of values. For the same simulations O and M, sea spray contributes considerably (up to 45%) to the total moisture flux and produces more humid layers than simulation C. When spray is included, the total moisture flux is in the middle of the observed range of values but it is slightly lower when it is not included.

Due to the spray-mediated latent heat flux, the O and M simulations develop large-scale structures of the residual stream-wise velocity found in ABLs driven by shear and buoyancy. On the other hand, simulation C shows streaky structures throughout the MABL which are usually observed

in neutral shear-dominated layers. For all simulations, lower-speed regions are strongly correlated with moister and colder regions in the surface layer, but only simulation M with the increased scalar fluxes preserves this up to the mid-MABL. The vertical velocity structure below the mid-MABL is not greatly influenced by the scalars concentrations within the large-scale structures of the residual stream-wise velocity, because buoyancy forces are negligible. However, differences are observed above that level.

The horizontal velocities variance is maximum near the surface due to shear, while the vertical velocity variance peaks at a height of about $0.15 Z_i$. The most intense fluctuations of potential temperature and water vapor mixing ratio occur near Z_i due to the entrainment process. Turbulence intensity, and individual momentum and moisture quadrant fluxes are stronger in simulation M simulation than those of simulation C, up to the point where the large-scale structures of the residual stream-wise velocity loses coherence. At the same time, while the normalized total momentum flux of M is equivalent to that of C, its net moisture transfer efficiency is increased 5–10% above the surface layer.

Simulation C produces scattered cloud structures throughout the domain with extremely low LWP ($<5\text{ gm}^{-2}$), while simulations M and O produce more extensive cloud decks. The highest liquid content is produced in simulation M, which is also characterized by the largest surface moisture flux. Despite the fact that all simulations produce optically-thin clouds, the differences in cloud properties have an impact on surface radiation. The simulation with the optically-thicker clouds (M) results in increased downward longwave emission and reduced shortwave radiation reaching the surface. Thus, the net effect on total surface radiation is a decrease of 30 Wm^{-2} (15 Wm^{-2}) compared to simulation C (O). These results indicate that modeling the thermodynamic impact of spray-mediated fluxes can considerably affect cloud characteristics and radiation patterns, which has substantial implications for climate studies.

The simulations used a value of 100 cm^{-3} for CCN concentration, which we consider to be a typical maritime value for the sea-spray particles that potentially act as CCN. According to Xu et al. (2022), the spray contribution to marine CCN is underestimated under strong wind conditions. A dynamic production of sea spray particles would be a more realistic contribution from this CCN source. However, this should be complemented by further research, including atmospheric chemistry in order to better understand the interactions of sea spray aerosol-derived CCN with other aerosols.

Appendix

See Figs. 10, 11, 12, 13, 14 and 15.

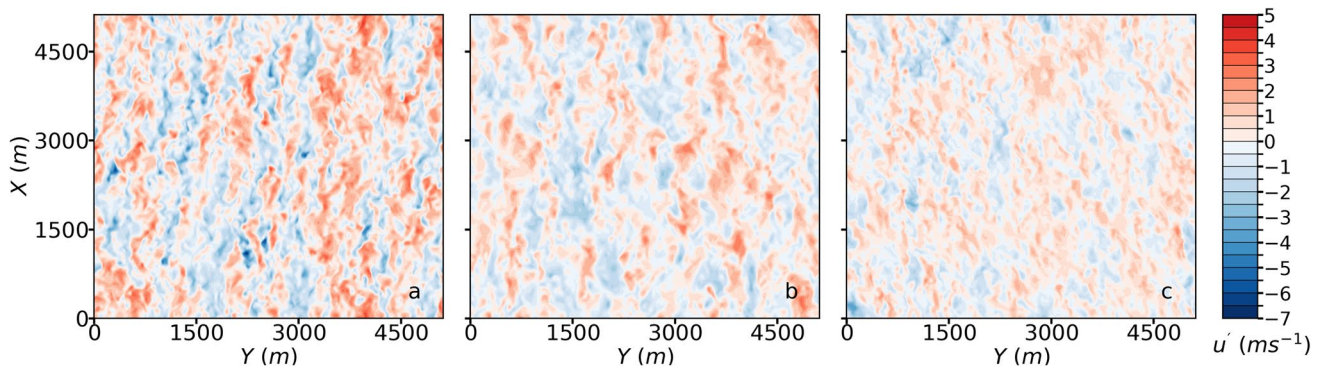


Fig. 10 Contours of the instantaneous residual vertical velocity u' of C simulation in the x - y plane at **a** $0.1 Z_i$; **b** $0.5 Z_i$; **c** $0.9 Z_i$

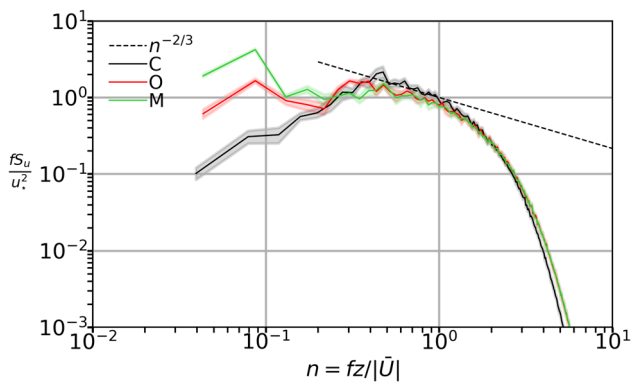


Fig. 11 Time-averaged, two dimensional horizontal spectra of stream-wise velocity u' at $z = 0.2 Z_i$ in the scaling of Kaimal et al. (1972)

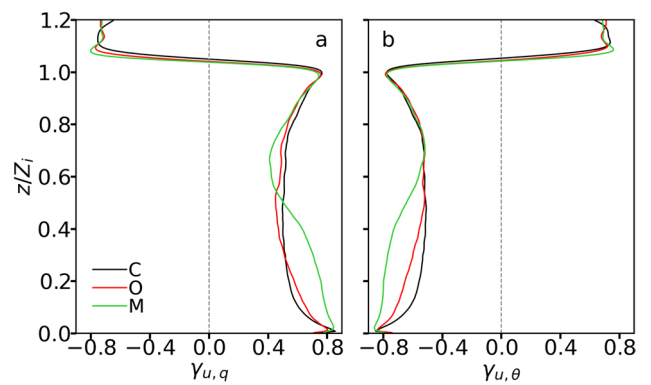


Fig. 12 Time-averaged vertical profiles of the correlation coefficient of **a** $\gamma_{u,q}$; **b** $\gamma_{u,\theta}$

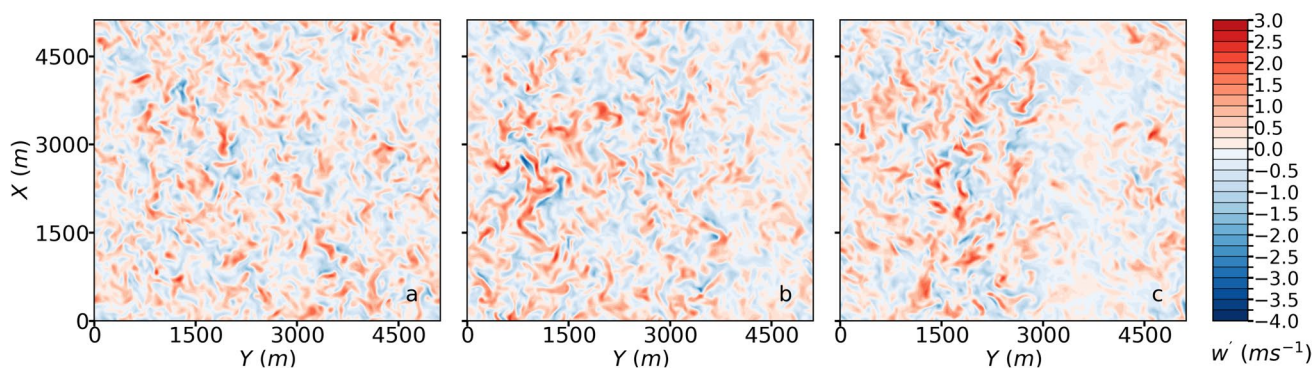


Fig. 13 Contours of the instantaneous residual vertical velocity w' at $0.6 Z_i$ in the x – y plane for simulation **a** C; **b** O; **c** M

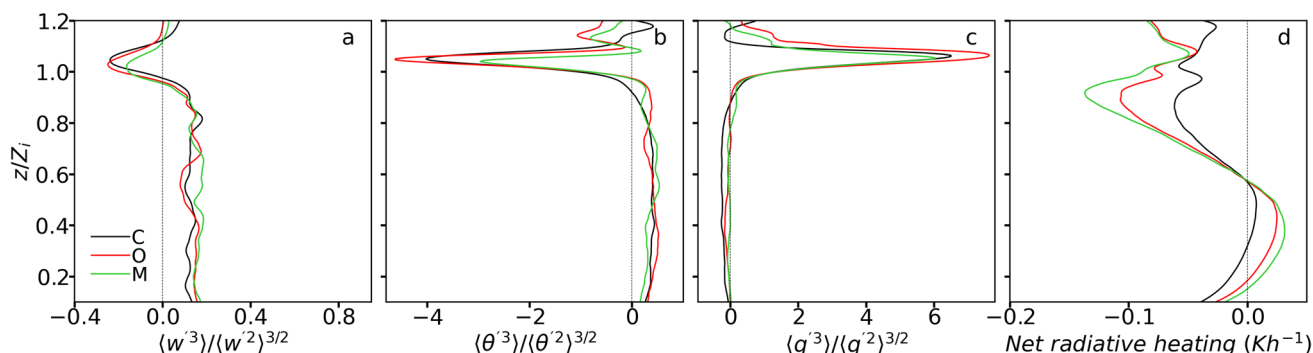


Fig. 14 Horizontally and temporally averaged normalized skewness profiles of the resolved **a** vertical component of wind speed **b** potential temperature **c** water vapor mixing ratio, and **d** net radiative heating

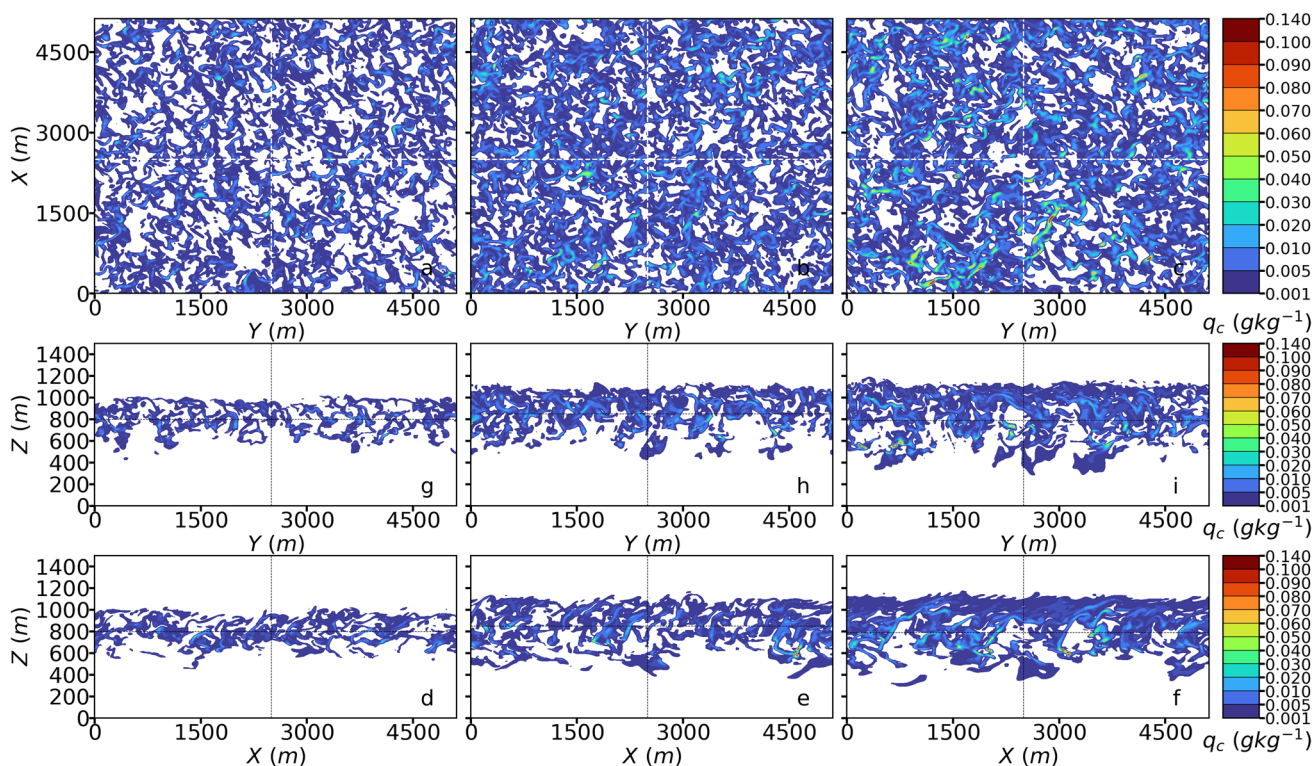


Fig. 15 In the first row, x – y plane contours of the instantaneous cloud vapor mixing ratio q_c at the height of each simulation's maximum averaged q_c (see Fig. 1f) **a** C; **b** O; **c** M. In the second row, the same as in the first row, but for the z – y plane ($x=2500$ m). In the third row, the same as in the second row, but for the z – x plane ($y=2500$ m)

Acknowledgements This work was supported by computational time granted from the National Infrastructures for Research and Technology S.A. (GRNET S.A.) in the National HPC facility—ARIS—under project ID “pr012034_thin”.

Author contributions Methodology: P. Portalakis and M. Tombrou; Formal Analysis: P. Portalakis; Investigation: P. Portalakis; Visualization: P. Portalakis; Writing—original draft: P. Portalakis; Writing—review and editing: M. Tombrou, J. Kalogiros and G. Sotiropoulou; Supervision: M. Tombrou and J. Kalogiros; Software: J. Savre and A. M.L. Ekman.

Funding This research is co-financed by Greece and the European Union (European Social Fund-ESF) through the Operational Programme «Human Resources Development, Education and Lifelong Learning» in the context of the project “Strengthening Human Resources Research Potential via Doctorate Research” (MIS-5000432), implemented by the State Scholarships Foundation (IKY).

Data availability Data sets generated during the current study are available from the corresponding author on reasonable request.

Declarations

Conflict of interest The authors declare that they have no conflict of interest.

References

- Albertson JD, Parlange MB (1999) Surface length scales and shear stress: implications for land-atmosphere interaction over complex terrain. *Water Resour Res* 35:2121–2132. <https://doi.org/10.1029/1999WR900094>
- Allan JD, Baumgardner D, Raga GB et al (2008) Clouds and aerosols in Puerto Rico—a new evaluation. *Atmos Chem Phys* 8:1293–1309. <https://doi.org/10.5194/ACP-8-1293-2008>
- Andreas EL (1995) The temperature of evaporating sea spray droplets. *J Atmos Sci* 52:852–862. [https://doi.org/10.1175/1520-0469\(1995\)052%3c0852:TTOESS%3e2.0.CO;2](https://doi.org/10.1175/1520-0469(1995)052%3c0852:TTOESS%3e2.0.CO;2)
- Andreas EL (2004) Spray stress revisited. *J Phys Oceanogr* 34:1429–1440. [https://doi.org/10.1175/1520-0485\(2004\)034%3c1429:SSR%3e2.0.CO;2](https://doi.org/10.1175/1520-0485(2004)034%3c1429:SSR%3e2.0.CO;2)
- Andreas EL (2005) Approximation formulas for the microphysical properties of saline droplets. *Atmos Res* 75:323–345. <https://doi.org/10.1016/j.atmosres.2005.02.001>
- Andreas EL, Emanuel KA (2001) Effects of sea spray on tropical cyclone intensity. *J Atmos Sci* 58:3741–3751. [https://doi.org/10.1175/1520-0469\(2001\)058%3c3741:EOSSOT%3e2.0.CO;2](https://doi.org/10.1175/1520-0469(2001)058%3c3741:EOSSOT%3e2.0.CO;2)
- Andreas EL, Wang S (2007) Predicting significant wave height off the northeast coast of the United States. *Ocean Eng* 34:1328–1335. <https://doi.org/10.1016/j.oceaneng.2006.08.004>
- Andreas EL, Persson POG, Hare JE (2008) A bulk turbulent air–sea flux algorithm for high-wind, spray conditions. *J Phys Oceanogr* 38:1581–1596. <https://doi.org/10.1175/2007JPO3813.1>
- Andreas EL, Mahrt L, Vickers D (2012) A new drag relation for aerodynamically rough flow over the ocean. *J Atmos Sci* 69:2520–2537. <https://doi.org/10.1175/JAS-D-11-0312.1>
- Andreas EL, Mahrt L, Vickers D (2015) An improved bulk air–sea surface flux algorithm, including spray-mediated transfer. *Q J R Meteorol Soc* 141:642–654. <https://doi.org/10.1002/qj.2424>
- Bao J-W, Fairall CW, Michelson SA, Bianco L (2011) Parameterizations of sea-spray impact on the air–sea momentum and heat fluxes. *Mon Weather Rev* 139:3781–3797. <https://doi.org/10.1175/MWR-D-11-00007.1>
- Barr BW, Chen SS, Fairall CW (2023) Sea-state-dependent sea spray and air–sea heat fluxes in tropical cyclones: a new parameterization for fully coupled atmosphere–wave–ocean models. *J Atmos Sci* 80:933–960. <https://doi.org/10.1175/JAS-D-22-0126.1>
- Belcher SE, Hunt JCR (1993) Turbulent shear flow over slowly moving waves. *J Fluid Mech* 251:109–148. <https://doi.org/10.1017/S0022112093003350>
- Bell MM, Montgomery MT, Emanuel KA (2012) Air–sea enthalpy and momentum exchange at major hurricane wind speeds observed during CBLAST. *J Atmos Sci* 69:3197–3222. <https://doi.org/10.1175/JAS-D-11-0276.1>
- Berg J, Patton EG, Sullivan PP (2020) Large-eddy simulation of conditionally neutral boundary layers: a mesh resolution sensitivity study. *J Atmos Sci* 77:1969–1991. <https://doi.org/10.1175/JAS-D-19-0252.1>
- Black PG, D’Asaro EA, Drennan WM et al (2007) Air–sea exchange in hurricanes: synthesis of observations from the coupled boundary layer air–sea transfer experiment. *Bull Am Meteorol Soc* 88:357–374. <https://doi.org/10.1175/BAMS-88-3-357>
- Bolton D (1980) The computation of equivalent potential temperature. *Mon Weather Rev* 108:1046–1053. [https://doi.org/10.1175/1520-0493\(1980\)108%3c1046:TCOEPT%3e2.0.CO;2](https://doi.org/10.1175/1520-0493(1980)108%3c1046:TCOEPT%3e2.0.CO;2)
- Bretherton CS, Wyant MC (1997) Moisture transport, lower-tropospheric stability, and decoupling of cloud-topped boundary layers. *J Atmos Sci* 54:148–167. [https://doi.org/10.1175/1520-0469\(1997\)054%3c0148:MTL TSA%3e2.0.CO;2](https://doi.org/10.1175/1520-0469(1997)054%3c0148:MTL TSA%3e2.0.CO;2)
- Bryan GH, Worsnop RP, Lundquist JK, Zhang JA (2017) A simple method for simulating wind profiles in the boundary layer of tropical cyclones. *Bound Layer Meteorol* 162:475–502. <https://doi.org/10.1007/s10546-016-0207-0>
- Charnock H (1955) Wind stress on a water surface. *Q J R Meteorol Soc* 81:639–640. <https://doi.org/10.1002/qj.49708135027>
- Chen X, Bryan GH, Zhang JA et al (2021) A framework for simulating the tropical-cyclone boundary layer using large-eddy simulation and its use in evaluating PBL parameterizations. *J Atmos Sci*. <https://doi.org/10.1175/JAS-D-20-0227.1>
- Clark TL (1979) Numerical simulations with a three-dimensional cloud model: lateral boundary condition experiments and multicellular severe storm simulations. *J Atmos Sci* 36:2191–2215. [https://doi.org/10.1175/1520-0469\(1979\)036%3c2191:NSWATD%3e2.0.CO;2](https://doi.org/10.1175/1520-0469(1979)036%3c2191:NSWATD%3e2.0.CO;2)
- Deardorff JW (1970) A numerical study of three-dimensional turbulent channel flow at large Reynolds numbers. *J Fluid Mech* 41:453–480. <https://doi.org/10.1017/S0022112070000691>
- Donelan MA (2004) On the limiting aerodynamic roughness of the ocean in very strong winds. *Geophys Res Lett* 31:L18306–L18306. <https://doi.org/10.1029/2004GL019460>
- Drennan WM (2003) On the wave age dependence of wind stress over pure wind seas. *J Geophys Res* 108:8062–8062. <https://doi.org/10.1029/2000JC000715>
- Drennan WM, Zhang JA, French JR et al (2007) Turbulent fluxes in the hurricane boundary layer. Part II: latent heat flux. *J Atmos Sci* 64:1103–1115. <https://doi.org/10.1175/JAS3889.1>
- Durran D, Weyn JA, Menchaca MQ (2017) Practical considerations for computing dimensional spectra from gridded data. *Mon Weather Rev* 145:3901–3910. <https://doi.org/10.1175/MWR-D-17-0056.1>
- Edson JB, Fairall CW (1998) Similarity relationships in the marine atmospheric surface layer for terms in the TKE and scalar variance budgets. *J Atmos Sci* 55:2311–2328. [https://doi.org/10.1175/1520-0469\(1998\)055%3c2311:SRITMA%3e2.0.CO;2](https://doi.org/10.1175/1520-0469(1998)055%3c2311:SRITMA%3e2.0.CO;2)
- Edson JB, Jampana V, Weller RA et al (2013) On the exchange of momentum over the open ocean. *J Phys Oceanogr* 43:1589–1610. <https://doi.org/10.1175/JPO-D-12-0173.1>

- Emanuel KA (1991) The theory of hurricanes. *Annu Rev Fluid Mech* 23:179–196. <https://doi.org/10.1146/annurev.fl.23.010191.001143>
- Fairall CW, Bradley EF, Hare JE et al (2003) Bulk parameterization of air–sea fluxes: updates and verification for the COARE algorithm. *J Clim* 16:571–591. [https://doi.org/10.1175/1520-0442\(2003\)016%3c0571:BPOASF%3e2.0.CO;2](https://doi.org/10.1175/1520-0442(2003)016%3c0571:BPOASF%3e2.0.CO;2)
- Foreman RJ, Emeis S (2010) Revisiting the definition of the drag coefficient in the marine atmospheric boundary layer. *J Phys Oceanogr* 40:2325–2332. <https://doi.org/10.1175/2010JPO4420.1>
- French JR, Drennan WM, Zhang JA, Black PG (2007) Turbulent fluxes in the hurricane boundary layer. Part I: momentum flux. *J Atmos Sci* 64:1089–1102. <https://doi.org/10.1175/JAS3887.1>
- Fu Q, Liou KN (1993) Parameterization of the radiative properties of cirrus clouds. *J Atmos Sci* 50:2008–2025. [https://doi.org/10.1175/1520-0469\(1993\)050%3c2008:POTRPO%3e2.0.CO;2](https://doi.org/10.1175/1520-0469(1993)050%3c2008:POTRPO%3e2.0.CO;2)
- Green BW, Zhang F (2015) Idealized large-eddy simulations of a tropical cyclone—like boundary layer. *J Atmos Sci* 72:1743–1764. <https://doi.org/10.1175/JAS-D-14-0244.1>
- Hao X, Shen L (2019) Wind–wave coupling study using LES of wind and phase-resolved simulation of nonlinear waves. *J Fluid Mech* 874:391–425. <https://doi.org/10.1017/jfm.2019.444>
- Hara T, Belcher SE (2004) Wind profile and drag coefficient over mature ocean surface wave spectra. *J Phys Oceanogr* 34:2345–2358. <https://doi.org/10.1175/JPO2633.1>
- Hara T, Sullivan PP (2015) Wave boundary layer turbulence over surface waves in a strongly forced condition. *J Phys Oceanogr* 45:868–883. <https://doi.org/10.1175/JPO-D-14-0116.1>
- Hare JE, Hara T, Edson JB, Wilczak JM (1997) A similarity analysis of the structure of airflow over surface waves. *J Phys Oceanogr* 27:1018–1037. [https://doi.org/10.1175/1520-0485\(1997\)027%3c1018:ASAOTS%3e2.0.CO;2](https://doi.org/10.1175/1520-0485(1997)027%3c1018:ASAOTS%3e2.0.CO;2)
- Hersbach H, Bell B, Berrisford P et al (2020) The ERA5 global reanalysis. *Q J R Meteorol Soc* 146:1999–2049. <https://doi.org/10.1002/qj.3803>
- Högström U (1988) Non-dimensional wind and temperature profiles in the atmospheric surface layer: a re-evaluation. *Bound Layer Meteorol* 42:55–78. <https://doi.org/10.1007/BF00119875>
- Holthuijsen LH, Powell MD, Pietrzak JD (2012) Wind and waves in extreme hurricanes. *J Geophys Res Oceans* 117:C09003. <https://doi.org/10.1029/2012JC007983>
- Janssen PAEM (1989) Wave-induced stress and the drag of air flow over sea waves. *J Phys Oceanogr* 19:745–754. [https://doi.org/10.1175/1520-0485\(1989\)019%3c0745:WISATD%3e2.0.CO;2](https://doi.org/10.1175/1520-0485(1989)019%3c0745:WISATD%3e2.0.CO;2)
- Kaimal JC, Wyngaard JC, Izumi Y, Coté OR (1972) Spectral characteristics of surface-layer turbulence. *Q J R Meteorol Soc* 98:563–589. <https://doi.org/10.1002/qj.49709841707>
- Kelly M, Wyngaard JC (2006) Two-dimensional spectra in the atmospheric boundary layer. *J Atmos Sci* 63:3066–3070. <https://doi.org/10.1175/JAS3769.1>
- Keperth J, Fairall C, Bao JW (1999) Modelling the interaction between the atmospheric boundary layer and evaporating sea spray droplets. In: Geernaert GL (ed) Air–sea exchange: physics, chemistry and dynamics. Atmospheric and oceanographic sciences library, vol 20. Springer, Dordrecht. https://doi.org/10.1007/978-94-015-9291-8_14
- Keperth JD, Schwendike J, Ramsay H (2016) Why is the tropical cyclone boundary layer not “well mixed”? *J Atmos Sci* 73:957–973. <https://doi.org/10.1175/JAS-D-15-0216.1>
- Khanna S, Brasseur JG (1998) Three-dimensional buoyancy- and shear-induced local structure of the atmospheric boundary layer. *J Atmos Sci* 55:710–743. [https://doi.org/10.1175/1520-0469\(1998\)055%3c0710:TDBASI%3e2.0.CO;2](https://doi.org/10.1175/1520-0469(1998)055%3c0710:TDBASI%3e2.0.CO;2)
- Khvorostyanov VI, Curry JA (2005) Fall velocities of hydrometeors in the atmosphere: refinements to a continuous analytical power law. *J Atmos Sci* 62:4343–4357. <https://doi.org/10.1175/JAS3622.1>
- Kudryavtsev VN (2006) On the effect of sea drops on the atmospheric boundary layer. *J Geophys Res* 111:C07020–C07020. <https://doi.org/10.1029/2005JC002970>
- Kudryavtsev VN, Makin VK (2001) The impact of air–flow separation on the drag of the sea surface. *Bound Layer Meteorol* 98:155–171. <https://doi.org/10.1023/A:1018719917275>
- Kudryavtsev VN, Makin VK (2007) Aerodynamic roughness of the sea surface at high winds. *Bound Layer Meteorol* 125:289–303. <https://doi.org/10.1007/s10546-007-9184-7>
- Kudryavtsev VN, Makin VK (2011) Impact of ocean spray on the dynamics of the marine atmospheric boundary layer. *Bound Layer Meteorol* 140:383–410. <https://doi.org/10.1007/s10546-011-9624-2>
- Kukulka T, Hara T (2008) The effect of breaking waves on a coupled model of wind and ocean surface waves. Part II: growing seas. *J Phys Oceanogr* 38:2164–2184. <https://doi.org/10.1175/2008JPO3962.1>
- Kukulka T, Hara T, Belcher SE (2007) A model of the air–sea momentum flux and breaking-wave distribution for strongly forced wind waves. *J Phys Oceanogr* 37:1811–1828. <https://doi.org/10.1175/JPO3084.1>
- Large WG, Pond S (1981) Open ocean momentum flux measurements in moderate to strong winds. *J Phys Oceanogr* 11:324–336. [https://doi.org/10.1175/1520-0485\(1981\)011%3c0324:OOMFMI%3e2.0.CO;2](https://doi.org/10.1175/1520-0485(1981)011%3c0324:OOMFMI%3e2.0.CO;2)
- Lee MJ, Kim J, Moin P (1990) Structure of turbulence at high shear rate. *J Fluid Mech* 216:561–583. <https://doi.org/10.1017/S0022112090000532>
- Lenschow DH, Wyngaard JC, Pennell WT (1980) Mean-field and second-moment budgets in a baroclinic. *Convect Bound Layer J Atmos Sci* 37(6):1313–1326. [https://doi.org/10.1175/1520-0469\(1980\)037%3c1313:MFASMB%3e2.0.CO;2](https://doi.org/10.1175/1520-0469(1980)037%3c1313:MFASMB%3e2.0.CO;2)
- Liu WT, Businger JA (1975) Temperature profile in the molecular sub-layer near the interface of a fluid in turbulent motion. *Geophys Res Lett* 2:403–404. <https://doi.org/10.1029/GL002i009p00403>
- Liu WT, Katsaros KB, Businger JA (1979) Bulk parameterization of air–sea exchanges of heat and water vapor including the molecular constraints at the interface. *J Atmos Sci* 36:1722–1735. [https://doi.org/10.1175/1520-0469\(1979\)036%3c1722:BPOASE%3e2.0.CO;2](https://doi.org/10.1175/1520-0469(1979)036%3c1722:BPOASE%3e2.0.CO;2)
- Lorsolo S, Schroeder JL, Dodge P, Marks F (2008) An observational study of hurricane boundary layer small-scale coherent structures. *Mon Weather Rev* 136:2871–2893. <https://doi.org/10.1175/2008MWR2273.1>
- Ma T, Sun C (2021) Large eddy simulation of hurricane boundary layer turbulence and its application for power transmission system. *J Wind Eng Ind Aerodyn* 210:104520–104520. <https://doi.org/10.1016/j.jweia.2021.104520>
- Mahrt L, Paumier J (1984) Heat transport in the atmospheric boundary layer. *J Atmos Sci* 41:3061–3075. [https://doi.org/10.1175/1520-0469\(1984\)041%3c3061:HTTIB%3e2.0.CO;2](https://doi.org/10.1175/1520-0469(1984)041%3c3061:HTTIB%3e2.0.CO;2)
- Makin VK (2005) A note on the drag of the sea surface at hurricane winds. *Bound Layer Meteorol* 115:169–176. <https://doi.org/10.1007/s10546-004-3647-x>
- Makin VK, Kudryavtsev VN (1999) Coupled sea surface-atmosphere model: 1. Wind over waves coupling. *J Geophys Res Oceans* 104:7613–7623. <https://doi.org/10.1029/1999JC900006>
- Makin VK, Kudryavtsev VN, Mastenbroek C (1995) Drag of the sea surface. *Bound Layer Meteorol* 73:159–182. <https://doi.org/10.1007/BF00708935>
- Maronga B, Li D (2022) An investigation of the grid sensitivity in large-eddy simulations of the stable boundary layer. *Bound Layer Meteorol* 182:251–273. <https://doi.org/10.1007/s10546-021-00656-8>

- Maronga B, Knigge C, Raasch S (2020) An improved surface boundary condition for large-eddy simulations based on Monin–Obukhov similarity theory: evaluation and consequences for grid convergence in neutral and stable conditions. *Bound Layer Meteorol* 174:297–325. <https://doi.org/10.1007/s10546-019-00485-w>
- Mellado JP (2017) Cloud-top entrainment in stratocumulus clouds. *Annu Rev Fluid Mech* 49(1):145–169. <https://doi.org/10.1146/annurev-fluid-010816-060231>
- Mellado JP, Bretherton CS, Stevens B, Wyant MC (2018) DNS and LES for simulating stratocumulus: better together. *J Adv Model Earth Sy* 10(7):1421–1438. <https://doi.org/10.1029/2018MS001312>
- Moeng C-H (1984) A large-eddy-simulation model for the study of planetary boundary-layer turbulence. *J Atmos Sci* 41:2052–2062. [https://doi.org/10.1175/1520-0469\(1984\)041%3c2052:ALESMF%3e2.0.CO;2](https://doi.org/10.1175/1520-0469(1984)041%3c2052:ALESMF%3e2.0.CO;2)
- Moeng C-H, Rotunno R (1990) Vertical-velocity skewness in the buoyancy-driven boundary layer. *J Atmos Sci* 47(9):1149–1162. [https://doi.org/10.1175/1520-0469\(1990\)047%3c1149:VVS-ITB%3e2.0.CO;2](https://doi.org/10.1175/1520-0469(1990)047%3c1149:VVS-ITB%3e2.0.CO;2)
- Moeng C-H, Sullivan PP (1994) A comparison of shear- and buoyancy-driven planetary boundary layer flows. *J Atmos Sci* 51:999–1022. [https://doi.org/10.1175/1520-0469\(1994\)051%3c0999:ACOSAB%3e2.0.CO;2](https://doi.org/10.1175/1520-0469(1994)051%3c0999:ACOSAB%3e2.0.CO;2)
- Moon I-J (2004) Effect of surface waves on Charnock coefficient under tropical cyclones. *Geophys Res Lett* 31:L20302–L20302. <https://doi.org/10.1029/2004GL020988>
- Moyer KA, Young GS (1991) Observations of vertical velocity skewness within the marine stratocumulus-topped boundary layer. *J Atmos Sci* 48(3):403–410. [https://doi.org/10.1175/1520-0469\(1991\)048%3c0403:OOVSW%3e2.0.CO;2](https://doi.org/10.1175/1520-0469(1991)048%3c0403:OOVSW%3e2.0.CO;2)
- Mueller JA, Veron F (2009) A sea state-dependent spume generation function. *J Phys Oceanogr* 39:2363–2372. <https://doi.org/10.1175/2009JPO4113.1>
- Mueller JA, Veron F (2014a) Impact of sea spray on air–sea fluxes. Part II: feedback effects. *J Phys Oceanogr* 44:2835–2853. <https://doi.org/10.1175/JPO-D-13-0246.1>
- Mueller JA, Veron F (2014b) Impact of sea spray on air–sea fluxes. Part I: results from stochastic simulations of sea spray drops over the ocean. *J Phys Oceanogr* 44:2817–2834. <https://doi.org/10.1175/JPO-D-13-0245.1>
- Nakanishi M, Niino H (2012) Large-eddy simulation of roll vortices in a hurricane boundary layer. *J Atmos Sci* 69:3558–3575. <https://doi.org/10.1175/JAS-D-11-0237.1>
- Nolan DS, Zhang JA, Stern DP (2009) Evaluation of planetary boundary layer parameterizations in tropical cyclones by comparison of in situ observations and high-resolution simulations of hurricane Isabel (2003). Part I: Initialization, maximum winds, and the outer-core boundary layer. *Mon Weather Rev* 137:3651–3674. <https://doi.org/10.1175/2009MWR2785.1>
- Peng T, Richter D (2019) Sea spray and its feedback effects: assessing bulk algorithms of air–sea heat fluxes via direct numerical simulations. *J Phys Oceanogr* 49:1403–1421. <https://doi.org/10.1175/JPO-D-18-0193.1>
- Peng T, Richter D (2017) Influence of evaporating droplets in the turbulent marine atmospheric boundary layer. *Bound Layer Meteorol* 165:497–518. <https://doi.org/10.1007/s10546-017-0285-7>
- Pedersen JG, Malinowski SP, Grabowski WW (2016) Resolution and domain-size sensitivity in implicit large-eddy simulation of the stratocumulus-topped boundary layer. *J Adv Model Earth Sy* 8(2):885–903. <https://doi.org/10.1002/2015MS000572>
- Powell MD, Vickery PJ, Reinhold TA (2003) Reduced drag coefficient for high wind speeds in tropical cyclones. *Nature* 422:279–283. <https://doi.org/10.1038/nature01481>
- Rauterkus R, Ansorge C (2020) Cloud-top entrainment in mixed-phase stratocumulus and its process-level representation in large-eddy simulation. *J Atmos Sci* 77(12):4109–4127. <https://doi.org/10.1175/JAS-D-19-0221.1>
- Richter DH, Sullivan PP (2013) Sea surface drag and the role of spray. *Geophys Res Lett* 40:656–660. <https://doi.org/10.1002/grl.50163>
- Richter DH, Wainwright CE (2023) Large-eddy simulation of sea spray impacts on fluxes in the high-wind boundary layer. *Geophys Res Lett*. <https://doi.org/10.1029/2022GL101862>
- Robinson SK (1991) Coherent motions in the turbulent boundary layer. *Annu Rev Fluid Mech* 23:601–639. <https://doi.org/10.1146/annurev.fl.23.010191.003125>
- Savre J, Ekman AML, Svensson G (2014) Technical note: Introduction to MIMICA, a large-eddy simulation solver for cloudy planetary boundary layers. *J Adv Model Earth Syst* 6:630–649. <https://doi.org/10.1002/2013MS000292>
- Seifert A, Beheng KD (2001) A double-moment parameterization for simulating autoconversion, accretion and selfcollection. *Atmos Res* 59–60:265–281. [https://doi.org/10.1016/S0169-8095\(01\)00126-0](https://doi.org/10.1016/S0169-8095(01)00126-0)
- Seifert A, Beheng KD (2006) A two-moment cloud microphysics parameterization for mixed-phase clouds. Part I: model description. *Meteorol Atmos Phys* 92:45–66. <https://doi.org/10.1007/s00703-005-0112-4>
- Shpund J, Zhang JA, Pinsky M, Khain A (2012) Microphysical structure of the marine boundary layer under strong wind and spray formation as seen from simulations using a 2D explicit microphysical model. Part II: The role of sea spray. *J Atmos Sci* 69:3501–3514. <https://doi.org/10.1175/JAS-D-11-0281.1>
- Shpund J, Zhang JA, Pinsky M, Khain A (2014) Microphysical structure of the marine boundary layer under strong wind and sea spray formation as seen from a 2D explicit microphysical model. Part III: parameterization of height-dependent droplet size distribution. *J Atmos Sci* 71:1914–1934. <https://doi.org/10.1175/JAS-D-12-0201.1>
- Smith SD (1988) Coefficients for sea surface wind stress, heat flux, and wind profiles as a function of wind speed and temperature. *J Geophys Res* 93:15467–15467. <https://doi.org/10.1029/JC093iC12p15467>
- Sroka S, Emanuel K (2021) A review of parameterizations for enthalpy and momentum fluxes from sea spray in tropical cyclones. *J Phys Oceanogr*. <https://doi.org/10.1175/JPO-D-21-0023.1>
- Stoll R, Porté-agel F (2006) Effect of roughness on surface boundary conditions for large-eddy simulation. *Bound Layer Meteorol* 118:169–187. <https://doi.org/10.1007/S10546-005-4735-2/METRICS>
- Stull RB (1988) An introduction to boundary layer meteorology. Springer, Dordrecht. <https://doi.org/10.1007/978-94-009-3027-8>
- Sullivan PP, McWilliams JC (2010) Dynamics of winds and currents coupled to surface waves. *Annu Rev Fluid Mech* 42:19–42. <https://doi.org/10.1146/annurev-fluid-121108-145541>
- Sullivan PP, Moeng C-H, Stevens B et al (1998) Structure of the entrainment zone capping the convective atmospheric boundary layer. *J Atmos Sci* 55:3042–3064. [https://doi.org/10.1175/1520-0469\(1998\)055%3c3042:SOTEZC%3e2.0.CO;2](https://doi.org/10.1175/1520-0469(1998)055%3c3042:SOTEZC%3e2.0.CO;2)
- Sullivan PP, McWilliams JC, Moeng C-H (2000) Simulation of turbulent flow over idealized water waves. *J Fluid Mech* 404:47–85. <https://doi.org/10.1017/S0022112099006965>
- Sullivan PP, Edson JB, Hristov T, McWilliams JC (2008) Large-eddy simulations and observations of atmospheric marine boundary layers above nonequilibrium surface waves. *J Atmos Sci* 65:1225–1245. <https://doi.org/10.1175/2007JAS2427.1>
- Sullivan PP, McWilliams JC, Patton EG (2014) Large-eddy simulation of marine atmospheric boundary layers above a spectrum

- of moving waves. *J Atmos Sci* 71:4001–4027. <https://doi.org/10.1175/JAS-D-14-0095.1>
- Sullivan PP, Banner ML, Morison RP, Peirson WL (2018) Turbulent flow over steep steady and unsteady waves under strong wind forcing. *J Phys Oceanogr* 48:3–27. <https://doi.org/10.1175/JPO-D-17-0118.1>
- Taylor PK, Yelland MJ (2001) The dependence of sea surface roughness on the height and steepness of the waves. *J Phys Oceanogr* 31:572–590. [https://doi.org/10.1175/1520-0485\(2001\)031%3c0572:TDOSSR%3e2.0.CO;2](https://doi.org/10.1175/1520-0485(2001)031%3c0572:TDOSSR%3e2.0.CO;2)
- Veron F (2015) Ocean spray. *Annu Rev Fluid Mech* 47:507–538. <https://doi.org/10.1146/annurev-fluid-010814-014651>
- Wang Y, Kepert JD, Holland GJ (2001) The effect of sea spray evaporation on tropical cyclone boundary layer structure and intensity. *Mon Weather Rev* 129:2481–2500. [https://doi.org/10.1175/1520-0493\(2001\)129%3c2481:TEOSSE%3e2.0.CO;2](https://doi.org/10.1175/1520-0493(2001)129%3c2481:TEOSSE%3e2.0.CO;2)
- Wex H, Dieckmann K, Roberts GC et al (2016) Aerosol arriving on the Caribbean island of Barbados: physical properties and origin. *Atmos Chem Phys* 16:14107–14130. <https://doi.org/10.5194/acp-16-14107-2016>
- Wood R (2012) Stratocumulus clouds. *Mon Weather Rev* 140:2373–2423. <https://doi.org/10.1175/MWR-D-11-00121.1>
- Worsnop RP, Bryan GH, Lundquist JK, Zhang JA (2017) Using large-eddy simulations to define spectral and coherence characteristics of the hurricane boundary layer for wind-energy applications. *Bound Layer Meteorol* 165:55–86. <https://doi.org/10.1007/s10546-017-0266-x>
- Wu J (1982) Wind-stress coefficients over sea surface from breeze to hurricane. *J Geophys Res* 87:9704–9704. <https://doi.org/10.1029/JC087iC12p09704>
- Wyngaard JC (1992) Atmospheric turbulence. *Annu Rev Fluid Mech* 24:205–234. <https://doi.org/10.1146/ANNUREV.FL.24.010192.001225>
- Xu W, Ovadnevaite J, Fossum KN, Lin C, Huang R-J, Ceburnis D, O'Dowd C (2022) Sea spray as an obscured source for marine cloud nuclei. *Nat Geosci* 15: 282–286. <https://doi.org/10.1038/s41561-022-00917-2>
- Yang D, Meneveau C, Shen L (2013) Dynamic modelling of sea-surface roughness for large-eddy simulation of wind over ocean wavefield. *J Fluid Mech* 726:62–99. <https://doi.org/10.1017/jfm.2013.215>
- Yelland M, Taylor PK (1996) Wind stress measurements from the open ocean. *J Phys Oceanogr* 26:541–558. [https://doi.org/10.1175/1520-0485\(1996\)026%3c0541:WSMFTO%3e2.0.CO;2](https://doi.org/10.1175/1520-0485(1996)026%3c0541:WSMFTO%3e2.0.CO;2)
- Zhang J (2007) An airborne investigation of the atmospheric boundary layer structure in the hurricane force wind regime. Dissertation, University of Miami. <https://scholarship.miami.edu/esplo/outputs/doctoral/An-Airborne-Investigation-of-the-Atmospheric-Boundary-Layer-Structure-in-the-Hurricane-Force-Wind-Regime/991031447299602976>. Accessed 19 June 2023
- Zhang JA (2010) Spectral characteristics of turbulence in the hurricane boundary layer over the ocean between the outer rain bands. *Q J R Meteorol Soc* 136:918–926. <https://doi.org/10.1002/qj.610>
- Zhang JA, Drennan WM (2012) An observational study of vertical eddy diffusivity in the hurricane boundary layer. *J Atmos Sci* 69:3223–3236. <https://doi.org/10.1175/JAS-D-11-0348.1>
- Zhang JA, Black PG, French JR, Drennan WM (2008) First direct measurements of enthalpy flux in the hurricane boundary layer: the CBLAST results. *Geophys Res Lett* 35:L14813–L14813. <https://doi.org/10.1029/2008GL034374>
- Zhang JA, Drennan WM, Black PG, French JR (2009) Turbulence structure of the hurricane boundary layer between the outer rainbands. *J Atmos Sci* 66:2455–2467. <https://doi.org/10.1175/2009JAS2954.1>
- Zheng Y, Rosenfeld D, Li Z (2018) The relationships between cloud top radiative cooling rates, surface latent heat fluxes, and cloud-base heights in marine stratocumulus. *J Geophys Res Atmos*. <https://doi.org/10.1029/2018JD028579>

Publisher's Note Springer Nature remains neutral with regard to jurisdictional claims in published maps and institutional affiliations.

Springer Nature or its licensor (e.g. a society or other partner) holds exclusive rights to this article under a publishing agreement with the author(s) or other rightsholder(s); author self-archiving of the accepted manuscript version of this article is solely governed by the terms of such publishing agreement and applicable law.